Article

Skin autonomous antibody production regulates host–microbiota interactions

https://doi.org/10.1038/s41586-024-08376-y

Received: 10 December 2023

Accepted: 8 November 2024

Published online: 11 December 2024

Open access

Check for updates

Inta Gribonika[1]✉, Victor I. Band[1], Liang Chi[1], Paula Juliana Perez-Chaparro[2], Verena M. Link[1], Eduard Ansaldo[1], Cihan Oguz[3], Djenet Bousbaine[4], Michael A. Fischbach[4] & Yasmine Belkaid[1,2,5]✉

The microbiota colonizes each barrier site and broadly controls host physiology[1]. However, when uncontrolled, microbial colonists can also promote inflammation and induce systemic infection[2]. The unique strategies used at each barrier tissue to control the coexistence of the host with its microbiota remain largely elusive. Here we uncover that, in the skin, host–microbiota symbiosis depends on the ability of the skin to act as an autonomous lymphoid organ. Notably, an encounter with a new skin commensal promotes two parallel responses, both under the control of Langerhans cells. On one hand, skin commensals induce the formation of classical germinal centres in the lymph node associated with immunoglobulin G1 (IgG1) and IgG3 antibody responses. On the other hand, microbial colonization also leads to the development of tertiary lymphoid organs in the skin that can locally sustain IgG2b and IgG2c responses. These phenomena are supported by the ability of regulatory T cells to convert into T follicular helper cells. Skin autonomous production of antibodies is sufficient to control local microbial biomass, as well as subsequent systemic infection with the same microorganism. Collectively, these results reveal a compartmentalization of humoral responses to the microbiota allowing for control of both microbial symbiosis and potential pathogenesis.

Metazoans exist as meta-organisms composed of the host itself and its symbiotic microbiota. This relationship is the most pronounced in barrier tissues, where diverse microorganisms colonize epithelial surfaces and broadly control host physiology and immunity[1]. A prerequisite for microbiota-tailored immune responses is that they must occur under non-inflammatory conditions. As such, we and others have shown that encounters with symbionts can lead to the homeostatic induction of diverse T cell responses that can broadly control tissue physiology, including tissue immunity and repair[3–5]. The skin is the largest and most exposed barrier site, and it harbours a plethora of microorganisms[1]. Of note, individuals with immunodeficiencies that affect immunoglobulin production are highly susceptible to skin infections[6], highlighting the importance of antibodies in the maintenance of skin barrier integrity. However, until recently, the skin was thought to be devoid of B cells and the role of antibodies in the control of skin–microbiota interaction remained largely unclear. Previous studies in humans uncovered high serum reactivity to the skin microbiota in the general population[7,8], supporting the idea that the microbiota may be able to promote antibody responses independently of infection. In addition, bacteria obtained from human skin swabs have been shown to be coated with immunoglobulins[9], and recent studies have also identified mature class-switched B cells in homeostatic human skin[10,11]. However, the extent to which B cell responses to the skin microbiota are induced in the absence of barrier breach and the role of these responses in constraining the microbiota within its physiological niche and preventing infection has not been addressed. Here we uncover a unique feature of skin immune autonomy in supporting a humoral response able to constrain the local biomass of the microbiota as well as subsequent systemic infection. Thus, this work reveals a function for the skin as a compartment in the absence of inflammation able to develop powerful antibody responses independently of secondary lymphoid organs.

Staphylococcus epidermidis induced antibodies

We previously showed that the skin of adult specific-pathogen-free (SPF) mice was permissive to long-term colonization with new commensals such as *S. epidermidis* (strain NIHLM087, clade A20)[12], as evidenced by stable resident colonies up to 200 days post-association[3] (Extended Data Fig. 1a). This non-inflammatory colonization was associated with the induction of commensal-specific T cells that boost local immunity and promote tissue repair[3,4]. Here we tested the possibility that skin colonization could also promote antibody responses. Following *S. epidermidis* topical association (TA), *S. epidermidis*-specific serum antibody responses were detected as early as 2 weeks and persisted for at least 200 days (Fig. 1a). IgG2b responses that dominated the *S. epidermidis* antibody repertoire developed first, and IgG1 and IgG2c responses increased gradually over the first 45 days post-association.

[1]Metaorganism Immunity Section, Laboratory of Host Immunity and Microbiome, National Institute of Allergy and Infectious Diseases, National Institutes of Health, Bethesda, MD, USA. [2]NIAID Microbiome Program, National Institute of Allergy and Infectious Diseases, National Institutes of Health, Bethesda, MD, USA. [3]Integrated Data Sciences Section, Research Technologies Branch, National Institute of Allergy and Infectious Diseases, National Institutes of Health, Bethesda, MD, USA. [4]Department of Bioengineering, Stanford University, Stanford, CA, USA. [5]Metaorganism Immunity Laboratory, Immunology Laboratory, Pasteur Institute, Paris, France. ✉e-mail: inta.gribonika@nih.gov; ybelkaid@niaid.nih.gov

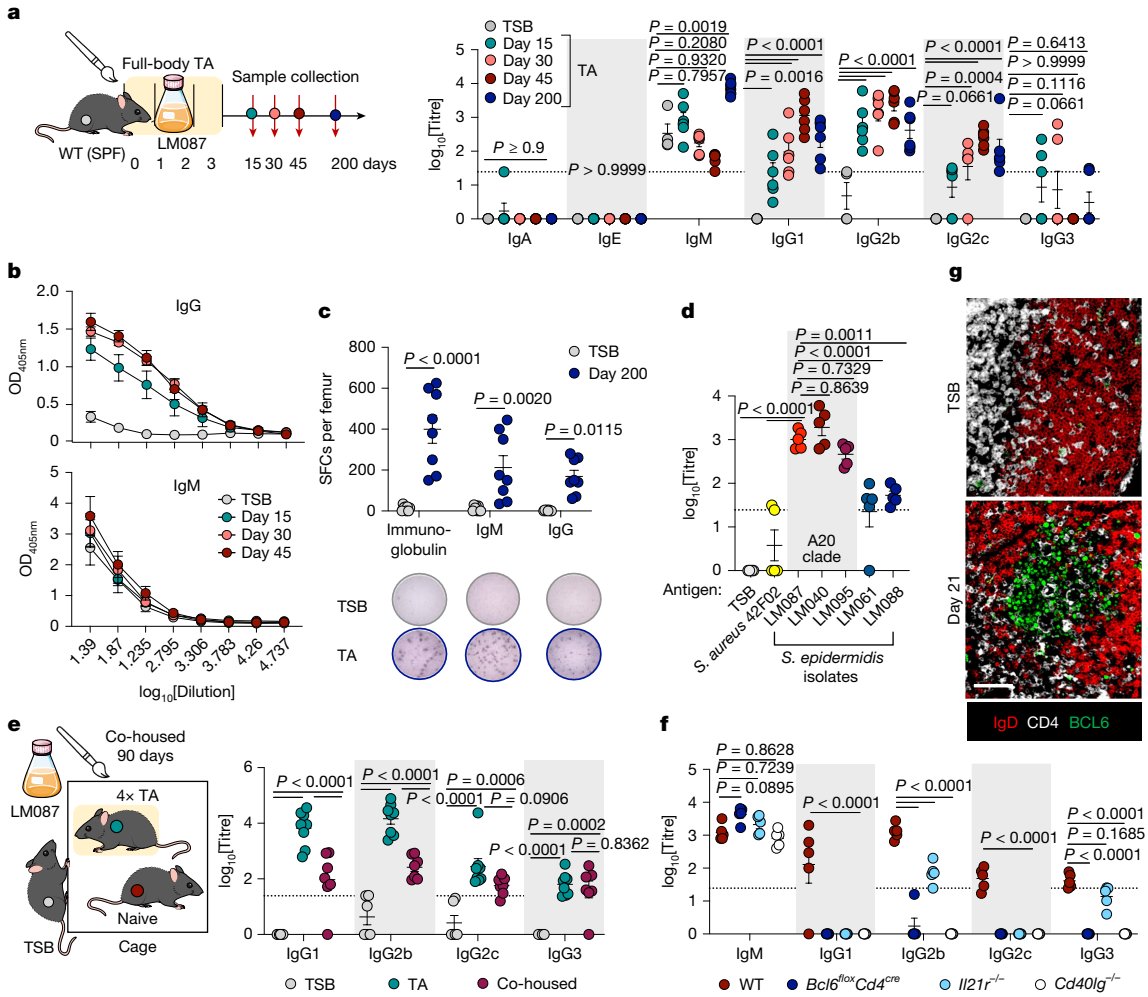

Fig. 1 | Skin colonization with commensal microorganisms induces systemic humoral immunity. a, Left: SPF C57BL/6 mice were associated (TA) with *S. epidermidis* isolate LM087 in Tryptic Soy Broth (TSB) for 4 consecutive days, and samples were collected as shown. Right: serum immunoglobulin reactivity to LM087 measured as $\log_{10}$ titres by enzyme-linked immunosorbent assay (ELISA); $n = 4$ (TSB) and 6 (TA). **b**, Enhancement of anti-*S. epidermidis* antibody affinity as the augmentation in the area under the curve; $n = 4$ (TSB), 5 (TA). **c**, *S. epidermidis*-specific total immunoglobulin, IgM and IgG spot-forming cells (SFCs) in bone marrow 200 days post-TA measured by enzyme-linked immunospot (Elispot) assay; $n = 8$. **d**, Serum IgG cross-reactivity of samples obtained from mice associated with LM087 60 days post-TA to antigens of various *S. epidermidis* isolates (LM087, LM040, LM095, LM061 and LM088) or *S. aureus* 42F02 or TSB measured as $\log_{10}$ titres by ELISA; $n = 5$ mice. **e**, Left: naive C57BL/6 mice were co-housed for 90 days with two or three 4 × TA C57BL/6 mice per cage as shown (TSB $n = 6$; TA $n = 8$; co-housed $n = 7$). Right: serum immunoglobulin reactivity to *S. epidermidis* in all mice measured as $\log_{10}$ titres by ELISA following co-housing for 90 days. **f**, WT, *Bcl6*^{flox}*Cd4*^{cre}, *Il21r*$^{-/-}$ and *Cd40lg*$^{-/-}$ mice were associated with LM087, and 45 days later serum reactivity to *S. epidermidis* was measured as $\log_{10}$ titres by ELISA; $n = 5$ mice. **g**, Representative cross-sectional confocal images of a B cell follicle (IgD$^+$ area in red; T cell zone in white) with (bottom) or without (top) a GC (BCL6$^+$ area in green) in a skin-draining cLN 21 days post-TA (bottom) or unassociated (TSB) control of BCL6–YFP reporter mouse; observation confirmed in more than 20 mice; cryosection thickness, 11 µm; scale bar, 50 µm. Results are representative of 2–3 independent experiments giving similar results. All data are presented as mean values ± s.e.m.; statistical significance was calculated by two-way analysis of variance (ANOVA) with Tukey's multiple comparison test (**a**,**e**,**f**), two-way ANOVA with Šidák's multiple comparison test (**c**) or ordinary one-way ANOVA with Dunnett's multiple comparison test (**d**). The schematics in **a**,**e** were created using graphical templates from Servier Medical Art under a Creative Commons licence CC BY 4.0 (https://creativecommons.org/licenses/by/4.0/).

A low level of *S. epidermidis* IgG3 response was also observed, but IgA and IgE were not detectable (Fig. 1a). Unlike IgM antibodies that were unaffected by *S. epidermidis* association and hence represented conserved natural immunity, IgG responses underwent amplification and affinity maturation as evidenced by an increased area under the curve over time (Fig. 1b). These responses were followed by the accumulation of *S. epidermidis*-specific antibody-secreting cells in the bone marrow, as observed 200 days post-TA, highlighting the induction of long-lived plasma cells (Fig. 1c). Association-induced antibodies were highly specific to the A20 clade-restricted *S. epidermidis* isolates and did not cross-react with isolates from other clades or different species of skin commensals such as *Staphylococcus aureus* (Fig. 1d). Of note, serum antibodies were also formed following *S. epidermidis* mono-colonization of germ-free mice, further supporting the specificity of these responses and highlighting the ability of a new colonizing microorganism to engage the immune system independently of pre-existing host microbiota (Extended Data Fig. 1b).

We next assessed whether skin microorganisms acquired passively could also promote a high-affinity antibody response. To this end, mice previously associated with *S. epidermidis* were co-housed with unassociated mice, and antibody responses were assessed in the latter group. Passively acquired microorganisms from neighbouring mice were sufficient to promote *S. epidermidis*-specific humoral immunity, revealing that, in adult mice, antibody responses to the microbiota can occur under physiological settings of microbial colonization (Fig. 1e).

To assess whether such a phenomenon was also true for microorganisms acquired early in life, we associated 3-day-old pups with *S. epidermidis* and assessed antibody responses 50 days later. Using this approach, we found that, in a similar manner to what was shown for effector T cells[13], neonatal colonization with *S. epidermidis* does not induce a humoral response despite sustained colonization. Thus, what we describe here are immune responses to a new commensal acquired post-early life and through the lifespan (Extended Data Fig. 1c).

In the gut, humoral responses to the microbiota can occur in both a T cell-dependent and a T cell-independent manner[14]. T cell-dependent responses are orchestrated by T follicular helper (T_{FH}) cells through interleukin-21 (IL-21) signalling and CD40–CD40L interactions in the germinal centre (GC)[15]. Thus, we assessed the response to the skin microbiota in *Bcl6*^{flox}*Cd4*^{cre} mice that specifically lack GC CD4$^+$ T cells (that is, T_{FH} and T follicular regulatory (T_{FR}) cells[16–18]), as well as in *Il21r*$^{-/-}$ and *Cd40lg*$^{-/-}$ mice. Whereas IgM responses were unchanged, we observed complete abrogation of the *S. epidermidis*-specific IgG response for all isotypes by 45 days post-TA in all three mouse models (Fig. 1f). These results supported the idea that the microbiota-specific IgG response required GC formation. Correspondingly, we observed a robust induction of BCL6$^+$ GCs in the skin-draining cervical lymph nodes (cLNs) 21 days post-association (Fig. 1g and Extended Data Fig. 1d,e). Thus, non-inflammatory TA with skin commensals can drive long-lasting systemic T cell-dependent IgG responses.

To test whether a humoral response could be observed in the context of other skin commensals, we topically associated SPF mice with a strain of *S. aureus* isolated from mouse skin[5] (Extended Data Fig. 1f) or with a natural mouse commensal, *Staphylococcus xylosus*[19] (Extended Data Fig. 1g). Colonization with both microorganisms led to specific serum IgG antibody responses. Thus, skin colonization with new commensals can drive long-lasting systemic IgG responses.

T_{FH} induction through regulatory T cell plasticity

The ability of skin commensals to induce potent IgG responses under homeostatic conditions prompted us to explore local events in the skin compartment. Systemic antibody responses against *S. epidermidis* were in correspondence with the gradual accumulation of B cells in the skin and, by day 45, the presence of *S. epidermidis*-specific antibody-secreting plasma cells (Fig. 2a,b and Extended Data Fig. 2a). Furthermore, the number of CD4$^+$ T cells expressing T_{FH} (PD-1$^+$CXCR5$^+$FOXP3$^-$) and T_{FR} (PD-1$^+$CXCR5$^+$FOXP3$^+$) phenotypic markers increased gradually during the first 3 weeks post-association in both the skin and the draining LNs (Fig. 2c and Extended Data Fig. 2b,c). Confocal imaging confirmed the expression of the classical GC markers PD-1 and CXCR5 in T cells in T helper (T_H)-rich areas of the dermis at 21 days post-TA (Fig. 2d). As the skin compartment lacks a naive cell pool (Extended Data Fig. 2b), we next explored the possibility that a fraction of commensal reactive T_{FH} cells may derive from local T cell plasticity. The skin contains one of the highest frequencies of FOXP3$^+$ regulatory T (T_{reg}) cells in the body[13,20], and in the gut, T_{reg} cells have been shown to downmodulate their suppressive signature and acquire a T_{FH} phenotype in the Peyer's patches[21,22]. The increase in skin T_{FH} cells post-association was accompanied by a notable decrease in the pool of local skin T_{reg} cells but not in the draining LNs (Fig. 2c and Extended Data Fig. 2c). To address the possibility that T_{reg} cells may be able to give rise to microbiota-reactive T_{FH} cells, we used a fate mapping strategy using *Foxp3*$^{eGFP\text{-}Cre\text{-}ERT2}$ × Rosa26^{tdTomato} mice allowing for tamoxifen (TAM)-inducible labelling of T_{reg} cell fate in vivo[23]. We first confirmed that this model is firm and stable as TAM-induced tdTomato labelling was observed only in the CD4$^+$ T cell compartment in skin, spleen, LN and Peyer's patches (Extended Data Fig. 2d,e). As expected, and independently of skin TA, approximately 30% of all T_{FH} cells in Peyer's patches were derived from T_{reg} cells[22] (Extended Data Fig. 2f), further strengthening previous observations on T_{reg} involvement in gut IgA induction[21,22,24]. Using this system, we further found that, by 21 days post-association, more than 90% of all skin and cLN T_{FH} cells were derived from T_{reg} cells that had lost their FOXP3 expression as evidenced by TAM-induced labelling (Fig. 2e). Thus, following skin colonization, the T_{reg} cells can give rise to the T_{FH} population—a phenomenon that could potentially promote local antibody responses. Further, the high frequency of converted cells raises the possibility that the T_{reg} repertoire might be biased towards defined microbial specificities.

This observation led us to assess the transcriptional signature of all skin CD4$^+$ T cells in the context of their lymphoid counterparts following TA and the potential connection between subsets through shared T cell receptor (TCR) specificities. Single-cell RNA sequencing (scRNA-seq) of fluorescence-activated cell sorting (FACS)-sorted cutaneous, splenic and LN CD4$^+$ T cells from wild-type (WT) mice at 21 days post-TA revealed 14 clusters with unique gene transcription (Extended Data Fig. 3a–c and Supplementary Table 1). Of note, scRNA-seq does not always reach the depth required to precisely identify all cell subsets. Further, most analyses of T cell subsets, and particularly those linked to GC reaction, have been performed in lymphoid organs. Thus, we subsequently annotated populations as T-like in cases in which signatures seemed incomplete or mixed with other distinct populations (Extended Data Fig. 3b,c and Supplementary Table 1). The reasoning for each annotation is summarized in Supplementary Table 1. The clusters P4, P5, P8 and P9 were enriched in a T_{reg} signature on the basis of *Foxp3* expression. These populations exhibited either a T_{FR} signature (*Bcl6* co-expression (P5, P9 and P8)) or a thymus-derived T_{reg} signature defined by *Ikzf2* and *Nrp1* expression (P8 and P4); at this time point, signatures associated with peripherally induced T_{reg} cells were not observed, suggesting that these cells may have already transdifferentiated into other cell populations such as T_{FH} cells. Indeed, the clusters P2 and P10 showed T_{FH} signatures on the basis of lineage-defining *Bcl6* expression. As these clusters shared signatures with either T_H17 cells (P2) or T_H1 cells (P10), we annotated these as type III or type I T_{FH} cells, respectively. The clusters P3 and P11 showed a naive phenotype on the basis of *Sell* expression.

The cluster P7 resembled an effector memory phenotype, whereas P13 was composed of recently activated cells on the basis of *Cd69* expression. The cluster P6 was enriched in proliferating cells on the basis of a high *Mki67* expression level, but we also noted some early T_{FH}-associated genes, and hence referred to this population as proliferating pre-T_{FH}-like cells. The clusters P1 and P14 exhibited T_H17-associated genes, although the level of *Rorc* expression was low (Extended Data Fig. 3c); therefore, these populations were annotated as T_H17-like. Finally, P12 expressed some T_H1-associated genes such as the master regulator *Tbx21*, but lacked the signature cytokine gene *Ifng*; therefore, we annotated this population as T_H1-like (Extended Data Fig. 3b,c and Supplementary Table 1). Skin samples were dominated by T_{FH}, T_{FR} and T_H17-like signatures, whereas, as expected, spleen and LN had mostly naive cells (Extended Data Fig. 3b,d). Owing to the experimental set-up, T_{FH} cells in the draining LN were under-represented, preventing us from directly comparing skin-to-LN subpopulations. However, the total skin TCR pool was almost exclusively unique and did not contain clonotypes found in LN or spleen (Extended Data Fig. 3d,e). Further, analysis of TCR clonotype sharing between populations in the skin revealed common TCRs among various T_{reg} and T_{FH} populations (Extended Data Fig. 3f), supporting the idea that, in response to a new skin microorganism, skin T_{reg} cells may be able to give rise to T_{FH} cells. Shared clones between skin T_{FR}- and T_{FH}-like cells suggest that T_{FH} could be derived from T_{FR} cells[25] (Extended Data Fig. 3f). However, T_{FR} cells are not present at the time of association (Fig. 2c), yet T_{FR} and T_{FH} cells appear in the skin with similar kinetics (Fig. 2c). Thus, our data support the notion of paralleled T_{FH} and T_{FR} differentiation possibly from the same T_{reg} or naive cell clone[26]. Together, these data suggest that the skin harbours its autonomous machinery for induction and maintenance of local CD4$^+$ T cell differentiation in GC T cells.

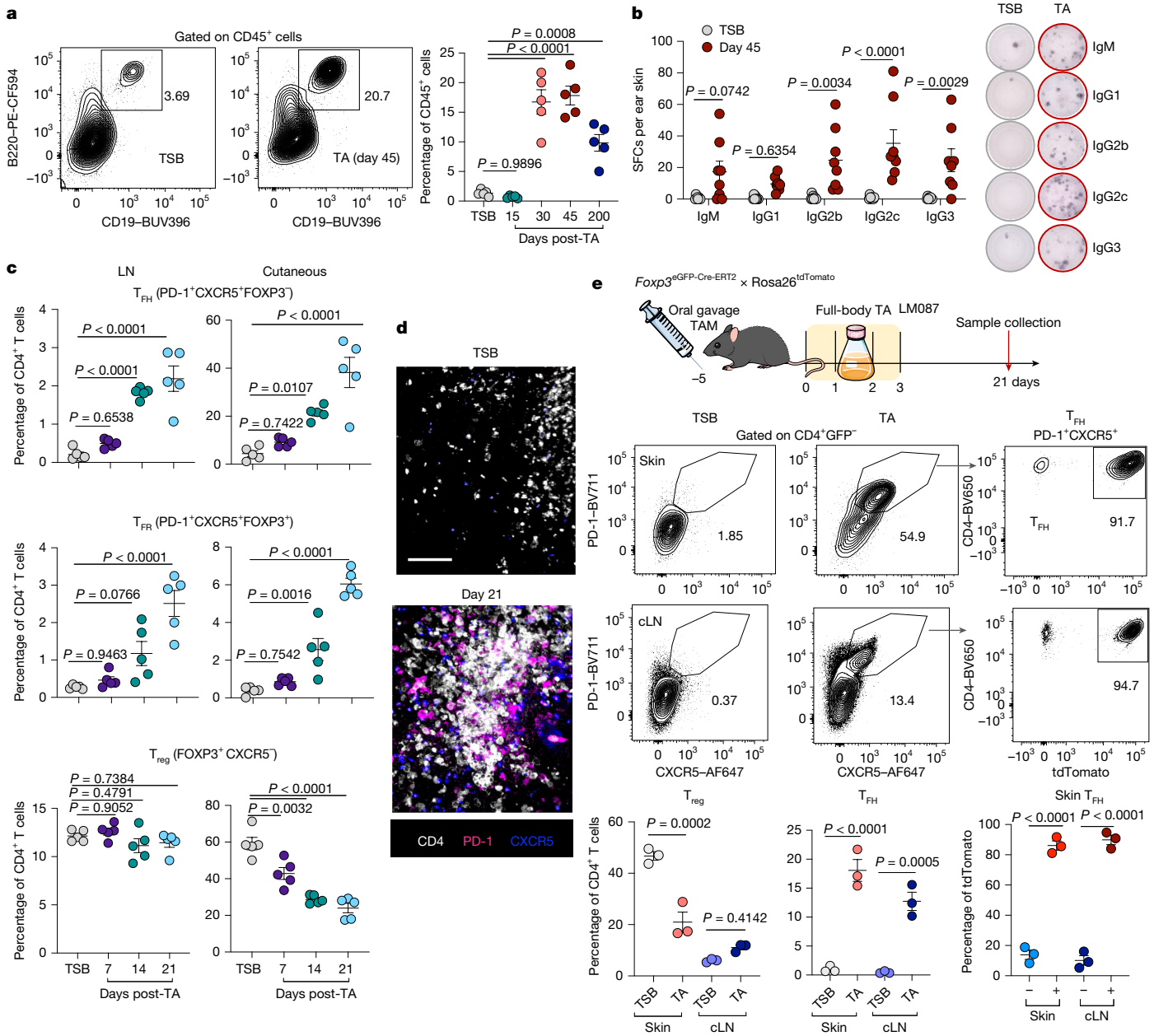

Fig. 2 | Skin colonization promotes cutaneous T_{FH} cells through T_{reg} plasticity. **a**,**b**, SPF C57BL/6 mice were associated (TA) with *S. epidermidis* isolate LM087 in TSB for 4 consecutive days, and samples were collected 15, 30, 45 and 200 days post-TA. **a**, Skin B cell ($B220^+CD19^+$) frequency of $CD45^+$ population analysed by flow cytometry in unassociated (TSB) or associated (TA) mice with two representative plots shown; $n = 5$. **b**, *S. epidermidis*-specific antibody-secreting cells in unassociated TSB skin and 45 days post-TA measured as spot-forming cells using Elispot assay; $n = 8$. **c**, WT mice were associated with *S. epidermidis* isolate LM087 for 4 consecutive days, and frequencies of T_{FH} ($PD\text{-}1^+CXCR5^+FOXP3^-$), T_{FR} ($PD\text{-}1^+CXCR5^+FOXP3^+$) and T_{reg} ($CXCR5^-FOXP3^+$) cells among all $CD4^+$ T cells were analysed by flow cytometry in cLN and skin of unassociated (TSB) and associated (day 7, 14 and 21) mice; $n = 5$. **d**, Cutaneous T_{FH} ($CD4^+$ (white), $PD\text{-}1^+$ (magenta), $CXCR5^+$ (blue)) in mice 21 days post-TA compared to that of unassociated (TSB) WT mice, as shown by confocal microscopy of ear dermis whole mount; scale bar, 50 µm; observation confirmed in five mice. **e**, Top: *Foxp3*$^{eGFP\text{-}Cre\text{-}ERT2}$ × Rosa26^{tdTomato} mice were treated with oral TAM 5 days before the 4× TA with LM087. Analysis of tdTomato fate-mapped T_{reg} differentiation into T_{FH} was performed 21 days after the association as shown. Representative flow plots of T_{FH} cells showing fate mapping strategy in skin and cLN (middle), and graphs depicting overall frequencies of green fluorescent protein (GFP; T_{reg}), T_{FH} among $CD4^+$ T cells and ±tdTomato T_{FH} cells (bottom) in individual mice; $n = 3$. Numbers in the flow plots (graphs) in **a**,**e** represent the gated population as a percentage of the parent gate (as indicated above the plots). Results are representative of 3–5 independent experiments giving similar results. All data are presented as mean values ± s.e.m.; statistical significance was calculated by two-way ANOVA with Šidák's multiple comparison test (**b**), ordinary one-way ANOVA with Dunnett's multiple comparison test (**a**), or ordinary one-way ANOVA with Tukey's multiple comparison test (**c**,**e**). The schematic in **e** was created using graphical templates from Servier Medical Art under a Creative Commons licence CC BY 4.0 (https://creativecommons.org/licenses/by/4.0/).

Formation of tertiary lymphoid organs

We next explored the possibility that, in the skin, commensal-induced T_{FH} cells could be organized within tertiary lymphoid structures. Although experimental and clinical studies have previously reported a GC phenotype associated with cutaneous malignancies and other skin inflammatory disorders[27–29], whether such structures could be formed under non-inflammatory conditions remains unclear. To address this

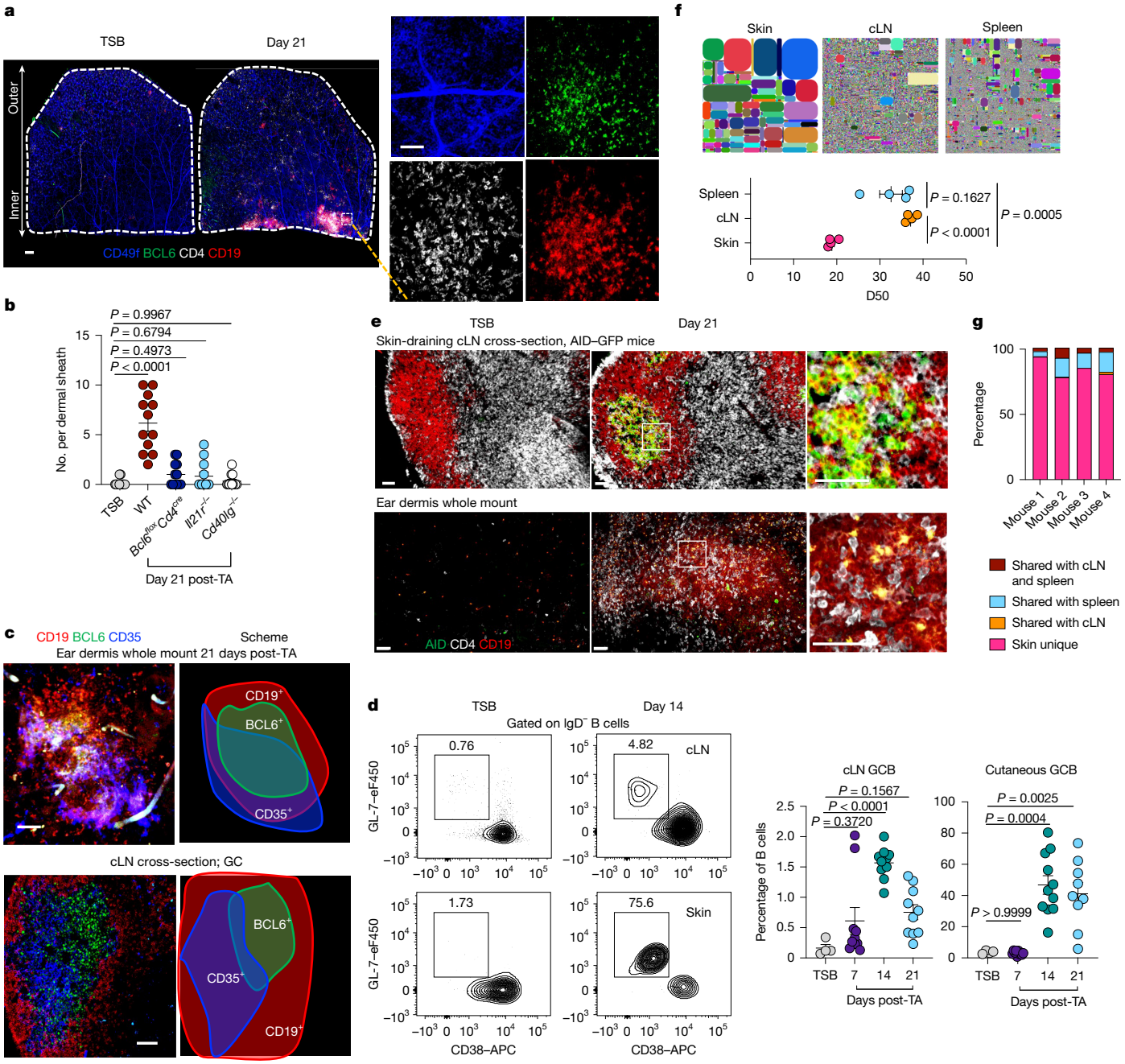

Fig. 3 | Skin colonization promotes formation of dermal TLOs. a, Cutaneous lymphocyte (CD4 (white), CD19 (red), BCL6 (green)) TLOs in ear dermis (CD49f (blue)) whole mount 21 days post-TA in comparison to unassociated (TSB) control of BCL6–YFP reporter mouse as shown by confocal tile scan of the entire ear; scale bars, 500 µm (left) and 50 µm (right). **b**, Enumeration of TLOs larger than 3,000 µm^3 per entire ear dermis whole mount in unassociated (TSB) and 21 day-associated WT (BCL6–YFP), *Bcl6*^{flox}*Cd4*^{cre}, *Il21r*$^{-/-}$ and *Cd40lg*$^{-/-}$ mice; $n = 12$. **c**, Dermal TLO whole mount (top left) and cLN cross-section (11 µm thickness; bottom left) 21 days post-TA (BCL6 (green), CD35 (blue), CD19 (red)), and schematic division into CD35$^+$ or CD35$^-$ zones as per CD35 staining of confocal images (right); scale bars, 30 µm (skin) and 50 µm (cLN); observation confirmed in five mice. **d**, Representative FACS plots (left) and frequencies of GCB cells (GL-7$^+$CD38$^-$; right) in cLN and skin of unassociated (TSB, $n = 4$) and *S. epidermidis*-associated (day 7, $n = 10$; day 14, $n = 10$ (cLN) and 11 (skin); day 21, $n = 10$ (cLN) and 9 (skin)) WT mice. Numbers in the flow plots (graphs) represent the gated population as a percentage of the parent gate (as indicated above the plots). **e**, AID–GFP reporter mouse topically associated with *S. epidermidis* and cLN cross-section (upper panel) or ear dermis whole mount (lower panel) compared with TSB (control) 21 days post-TA. Samples stained for CD4 (white), CD19 (red) and AID (GFP). Cross-section thickness: 11 µm. Scale bars, 40 µm (cLN) and 50 µm (skin). The result is representative of five independent experiments. **f**,**g**, BCR-seq of total RNA extracted from skin, cLN and spleen of WT mice 30 days post-TA with LM087, $n = 4$. **f**, Representative BCR tree maps (top) and BCR repertoire diversity calculated as D50 per organ (bottom). **g**, Bar graph showing total skin BCR clone overlap with BCRs in spleen and/or cLN in individual mice. Results are representative of 2–5 independent experiments. All data are presented as mean values ± s.e.m.; statistical significance calculated by ordinary one-way ANOVA with Dunnett's multiple comparison test (**b**), or ordinary one-way ANOVA with Tukey's multiple comparison test (**d**,**f**).

point, we utilized a BCL6–YFP reporter mouse model, allowing for the visualization of GC T and GC B (GCB) cells[30,31]. TA with *S. epidermidis* recruited BCL6-expressing B cells and CD4$^+$ T cells within large dermal tertiary lymphoid organs (TLOs; Fig. 3a). Skin microbiota-induced dermal TLOs also depended on critical determinants of GC reaction such as IL-21R, CD40L or T_{FH} cells (Fig. 3b).

Classical GCs are subdivided into the light and dark zone by follicular dendritic cells that express CD35 (ref. 32). This feature was confirmed in the skin-draining LN, where commensal colonization-induced GC contained a $CD35^+$ light zone and a $CD35^-$ dark zone (Fig. 3c (bottom)). As visualized in the dermis whole-mount confocal image and its schematic recapitulation, dermal TLOs were also subdivided into two distinct zones on the basis of CD35 staining (Fig. 3c (top)). Collectively, these data pointed to the ability of commensal-induced TLOs to directly promote antibody responses to microbiota-derived antigens. Consistent with our hypothesis, our observations showed that TA with *S. epidermidis* gradually expanded the GCB cell pool in both the draining LNs and in the skin, with as many as 80% of all B cells acquiring a canonical $IgD^-CD38^-GL\text{-}7^+$ GCB cell phenotype by 14 days post-association (Fig. 3d and Extended Data Fig. 4a). Owing to a lack of specific tools, we could not test GCB specificity directly. However, a skin GCB phenotype was also induced and maintained following mono-colonization of germ-free mice, further supporting the idea that skin GCB cells are *S. epidermidis* specific (Extended Data Fig. 4b).

To address whether skin-intrinsic B cells also have the potential to undergo class-switch recombination and affinity maturation, we assessed the expression of B cell-specific enzyme activation-induced cytidine deaminase (AID)[33,34]. In the cLN and as expected, confocal imaging revealed AID expression in the B cell follicle by day 7 post-association (Extended Data Fig. 4c). In a parallel manner, B cells also upregulated AID expression in the skin (Extended Data Fig. 4d). AID expression was maintained at both sites, as evidenced by confocal microscopy of LN sections and skin dermis whole mounts 21 days post-association (Fig. 3e). To confirm that B cells isolated from the skin were not contaminants from circulation, we performed in vivo anti-CD45 labelling shortly before tissue collection (Extended Data Fig. 4e). As evidenced in our single-cell tissue preparations, only up to 4% of all skin B cells were derived from circulation, confirming that cutaneous B cells are tissue residents. To evaluate the expression level of common GCB markers including Ki-67, BCL6, CD95, AID, GL-7 and CD44, we then compared GCB cells and IgD^+ (naive) B cells in skin and LN 21 days post-TA (Extended Data Fig. 4f,g). As expected, IgD^+ cells at both sites expressed IgD and CD38 and did not express any GCB-associated markers. On the other hand, LN and skin GCB cells significantly upregulated all GCB-associated markers. Whereas skin GCB cells had significantly lower expression levels of BCL6, Ki-67 and AID, the level of CD95 expression was higher in the skin than in LN. Thus, the cutaneous population of GCB cells was phenotypically comparable to the LN counterparts, albeit with differences in expression level (Extended Data Fig. 4f,g). Together, these data support the idea that TA with a skin commensal can promote de novo formation of functional GC-like structures in the skin dermis.

Next we characterized the skin B cell receptor (BCR) repertoire post-association and how such repertoire related to B cell clones found in lymphoid organs. To this end, we performed BCR sequencing (BCR-seq) of whole-tissue RNA samples that allowed us to capture the entire B cell repertoire including naive, activated, memory, GCB and plasma cells from skin, spleen and skin-draining LN 30 days post-association with *S. epidermidis* (Fig. 3f,g, Extended Data Fig. 4h–j and Supplementary Tables 2 and 3). This experimental approach did not allow for comparison of distinct subpopulations such as GCB cells between the skin and the LN but allowed us to analyse the B cell repertoire in its entirety. As expected, on the basis of BCR tree maps and the D50 value, the skin BCR repertoire diversity was significantly lower than that of spleen or LN (Fig. 3f); skin B cells had a low diversity with many expanded clones, whereas spleen and LN had only occasional expanded clones with very high diversity. As seen with LN and spleen samples, the closer the D50 score to 50, the more diverse the library. In support of lower diversity and more expanded clones (Fig. 3f), our findings showed that skin BCRs had a higher mutation burden when compared to lymphoid organs, with close to 80% of all skin BCRs having acquired somatic hypermutations, indicative of active B cell engagement (Extended Data Fig. 4h and Supplementary Tables 2 and 3). To assess the potential contribution of lymphoid B cells to the skin B cell repertoire, we looked at total skin BCRs (Fig. 3g) and total mutated skin BCRs for any indication of shared clonotypes with LN and spleen (Extended Data Fig. 4i). In both cases, close to 90% of clonotypes were unique to the skin compartment, with only 10–15% shared with the spleen. A minor fraction of all skin B cells shared clones with splenic IgM B cells (Extended Data Fig. 4j), pointing to the possibility that gut microbiota-reactive B cells in the spleen[35] may be able to seed the skin post-microbial association.

Of note, below 1% of all skin BCR clonotypes were shared uniquely with LN, supporting the model that GCB cell responses in skin and LN may be independent and follow distinct trajectories (Fig. 3g, Extended Data Fig. 4i and Supplementary Tables 2 and 3). These data further complement the unique signature of skin $CD4^+$ T cells compared to LN (Extended Data Fig. 3e) and together support the notion that dermal TLOs could be formed and maintained independently of classical GCs in the LN.

Langerhans cell-mediated response

TLO formation is a general response to skin colonization observed with several skin microorganisms, including the mouse skin commensal *S. xylosus* (Extended Data Fig. 5a), indicating that the tissue can respond to new encounters with distinct members of the microbiota.

TLO formation requires gateways for lymphocyte trafficking[36]. High endothelial venules (HEVs) are specialized postcapillary venules found in lymphoid tissues that support high levels of lymphocyte extravasation from the blood. Mature HEVs express PNAd, an L-selectin ligand that can be detected by the prototypic antibody MECA-79 (refs. 37,38). To test whether dermal TLOs are associated with HEVs, confocal microscopy was performed on the skin dermis whole mount 45 days post-association (Extended Data Fig. 5b). This approach revealed that skin TLOs were strongly associated with HEVs that were fully embedded within these structures. HEVs were detected only in association with TLOs and not observed in control mice (Extended Data Fig. 5b).

This observation prompted us to explore the kinetics of TLO formation. By day 7 post-association, lymphocytes began to form ring-like structures around hair follicles, and by day 14, they were organized in dense clusters, eventually forming large BCL6-expressing TLOs by day 21 (Extended Data Fig. 5c). The hair follicle represents the primary site of microbial colonization[39], and as such it is a potential privileged site for microbial antigen capture and presentation. In support of this, confocal imaging revealed that a fraction of hair follicles and associated TLOs were actively surveyed by dendritic cells (visualized by CD11c) following *S. epidermidis* TA (Extended Data Fig. 5d). Notably, dermal TLOs were heavily enriched in CXCL13—a chemokine associated with the follicular dendritic cell network in classical GCs[40,41]—and were patrolled by Langerin-expressing cells found at the centre of TLOs and in association with the hair follicle linked to the TLOs (Extended Data Fig. 5e and Supplementary Video 1). Langerhans cells (LCs) are the most abundant antigen-presenting cells in the skin[42,43], and these cells are ideally positioned to surveil and respond to microbial encounters. Although previous work proposed a role for LCs in orchestrating GC formation in skin-draining LN in the context of vaccination or infection[44–46], whether LCs contribute to responses to the microbiota has not been addressed. We therefore utilized the huLang-DTR mouse model that allows for specific depletion of LCs following administration of diphtheria toxin without affecting any other tissue-resident dendritic cell population[47] (Extended Data Fig. 6a,d). Short-term depletion of LCs before the TA was sufficient to significantly reduce the induction of cutaneous T_{FH} cells in the skin (Extended Data Fig. 6b). Further, LC depletion completely abrogated the induction of all IgG isotypes to *S. epidermidis* (Extended Data Fig. 6c). Thus, LCs play a central role in

promoting T_{FH} responses and humoral immunity in the skin. Tissue cytokine availability is an important aspect of humoral response[48]. LC depletion before TA significantly altered the absolute numbers of IL-4- and interferon-γ (IFNγ)-secreting $CD4^+$ T cells in the skin—cytokines required for IgG1 and IgG2c or IgG3 class-switch recombination, respectively (Extended Data Fig. 6e). Thus, LCs may contribute to antibody responses to the microbiota through several mechanisms including antigen presentation and the promotion of a cytokine milieu favourable to class switching.

Skin autonomous antibody production

The observation that skin $CD4^+$ T cells and B cells did not share clones with lymphoid organs (Fig. 3g and Extended Data Figs. 3e and 4i) prompted us to test the possibility that the skin tissue may be able to support a humoral response independently of secondary lymphoid structures. To address this point, we first used treatment with fingolimod (FTY720)—an agonist of the sphingosine 1-phosphate 1 receptor that promotes lymphocyte sequestration[49]. FTY720 treatment was started 2 days before the TA and continued every other day throughout the experiment (Fig. 4a and Extended Data Fig. 7a). Lymphocyte sequestration led to a significant decrease in *S. epidermidis*-specific serum IgG1 and IgG3, indicating that these responses are dependent on classical GC reaction in LNs. By contrast, IgG2b responses, although reduced, were still very much detectable, and IgG2c responses were unaffected by FTY720 treatment (Fig. 4a). In agreement, B cell phenotypic analysis revealed a comparable level of IgG2b expression between control and FTY720 treatment (Extended Data Fig. 7a). Short-term FTY720 treatment did not affect serum reactivity to *S. epidermidis* with any isotype (Extended Data Fig. 7b), indicating that both early responses (all isotypes) and late responses (IgG2b and IgG2c antibodies) can be sustained in the skin compartment independently of lymphocyte trafficking to the LNs (Fig. 4a).

As dendritic cell migration to the draining LNs is CCR7 dependent[50], we then further tested our hypothesis using *Ccr7*$^{-/-}$ mice. Similarly to what we observed in the context of the FTY720 experiment, *Ccr7*$^{-/-}$ mice had significantly reduced IgG1 and IgG3 responses compared to WT, whereas IgG2b responses were only slightly reduced and IgG2c responses were unaffected (Extended Data Fig. 7c). Thus, dendritic cell migration to the LN is not required to produce the microbiota-specific IgG2b and IgG2c antibodies. In line with this observation, no differences in IL-4 or IFNγ were observed in both FTY720-treated mice and *Ccr7*$^{-/-}$ mice compared to controls (Extended Data Fig. 7d).

To further address the skin autonomous humoral response, we performed splenectomy on *Lta*$^{-/-}$ mice to fully abrogate the potential contribution of all professional lymphoid organs[51]. At 30 days post-splenectomy or sham surgery, mice were topically associated, and serum responses were assessed 35 days later (Fig. 4b). Splenectomy alone and sham surgery had no impact on antibody responses (Fig. 4b). In the complete absence of secondary lymphoid organs, IgG1 and IgG3 responses were abrogated further, supporting the idea that LNs are required to produce these two isotypes in response to the skin microbiota colonization. On the other hand, in the absence of secondary lymphoid structures, IgG2b responses, although reduced, were still detectable, and IgG2c responses were unaffected (Fig. 4b). In support of this observation, TLOs were still able to form in response to microbial association in the complete absence of secondary lymphoid organs (Fig. 4c). In a comparable manner to those in WT mice (Extended Data Fig. 5e), CXCL13-expressing cells were enriched in the TLO and around the hair follicle in *Lta*$^{-/-}$ mice (Extended Data Fig. 7e). Of note, CXCL13-expressing cells were $CD45^-$, pointing to a stromal origin to produce this central chemokine. Further, hair follicles were also surrounded by HEVs, highlighting the redundancy of LTα in dermal TLO formation (Extended Data Fig. 7e). To test whether *Lta*$^{-/-}$ mice could also sustain cutaneous GCB cells, we performed cell phenotyping 14 days after association (Extended Data Fig. 7f). Following association, *Lta*$^{-/-}$ mice accumulated a robust cutaneous GCB population in the skin but not in the spleen (Extended Data Fig. 7f). Notably, cutaneous GCB cells in *Lta*$^{-/-}$ mice were phenotypically comparable to those developing in WT mice (Extended Data Fig. 7g). These data further support the idea that the skin can prime and sustain local antibody development.

Swabbing the skin post-association revealed that *S. epidermis*-specific antibodies could be readily detected at the skin surface (Fig. 4d). Further highlighting the dichotomy of responses between the skin and the LNs, skin swabs predominantly contained IgG2b antibodies with minor detection of IgG2c, but not IgG1 or IgG3 (Fig. 4d). By contrast, *S. epidermidis*-specific IgG antibodies were not detected at the skin surface of *Bcl6*^{flox}*Cd4*^{cre}-associated mice, supporting the T cell-dependent mechanism of the response (Fig. 4e). Notably, topical antibody responses were intact in *Lta*$^{-/-}$ mice, further highlighting the autonomous ability of the skin to produce antibodies (Fig. 4e). Of note, these IgG2b antibodies were generated in dermal TLOs, as evidenced by ear dermis whole mount confocal microscopy 45 days after association (Extended Data Fig. 7h). Thus, *S. epidermidis*-specific IgG1 and IgG3 responses require a professional inductive environment, whereas the skin can develop dermal TLOs independently of lymphoid structures and mount and release IgG2b and IgG2c responses both locally and systemically. An alternative stimulus for TLO formation in the absence of LTα is tumour necrosis factor (TNF) signalling[52]. However, TA of *Tnfa*$^{-/-}$ mice did not show any impairments in systemic antibody production to *S. epidermidis* or dermal TLO formation (Extended Data Fig. 7i), thus indicating that alternative stimuli might be involved to sustain skin B cell responses.

The observation that humoral responses could be mounted in *Lta*$^{-/-}$ mice allowed us to assess the transcriptional signature of skin B cells independently of any possible contribution from secondary lymphoid organs. The scRNA-seq of FACS-sorted $CD19^+B220^+$ B cells from *Lta*$^{-/-}$ mice at 14 days post-TA allowed us to identify nine clusters with unique gene transcription that partially overlapped with known B cell signatures (Fig. 4f,g, Extended Data Figs. 3a and 8a,b and Supplementary Table 4). Given the shallow depth of capture of gene expression by this technique and limited literature on tissue B cells, we subsequently annotated populations as B-like. Skin B cells harboured distinct transcriptional signatures that can be associated with the regulation of humoral immunity (Fig. 4f, Extended Data Fig. 8a and Supplementary Table 4). Upregulation of GC-associated genes such as *Cxcr5*, *Junb*, *Myc*, *Cd83*, *Egr1*, *Nfkbia* (cluster P4), *Pou2af1* (cluster P2), *Foxo1* and *Fcer2a* (cluster P8) was observed in various populations, potentially indicating distinct stages of B cell commitment to GC reaction, although classical GC repressors such as *Gpr183* (cluster P4) were also expressed, indicating that tissue B cells may be differentially regulated from their lymphoid counterparts (Extended Data Fig. 8a and Supplementary Table 4). Despite AID expression (Fig. 3e and Extended Data Fig. 4d–f), with this approach and at this time point, we did not detect expression of *Aicda* (a gene that encodes the AID enzyme), probably owing to the transient nature of the enzyme or difference in the kinetics of its expression in B cells from *Lta*$^{-/-}$ compared to WT mice. Notably, tissue B cells lacked a naive B cell signature as none of the populations had *Ighd* expression that encodes for the naive cell marker IgD (Extended Data Fig. 8a). It is important to note that precursor transcripts of each B cell population were already present at homeostasis (tryptic soy broth (TSB)), but TA treatment expanded these cells to sizeable populations (Fig. 4f). Whereas immunoregulatory (P7), memory-like (P8), MZB-like (P6) and dying B-like (P5) cells remained stable among treatments, the TA strongly favoured expansion of activated (P1), pre-GCB-like (P0), follicular B-like (P3), mature B-like (P2) and, most importantly, GCB-like (P4) cells (Fig. 4g and Extended Data Fig. 8b). Collectively, these data indicate that skin B cells can readily respond to cutaneous antigens, independently of secondary lymphoid organ contribution, and transcriptionally recapitulate their lymphoid counterparts.

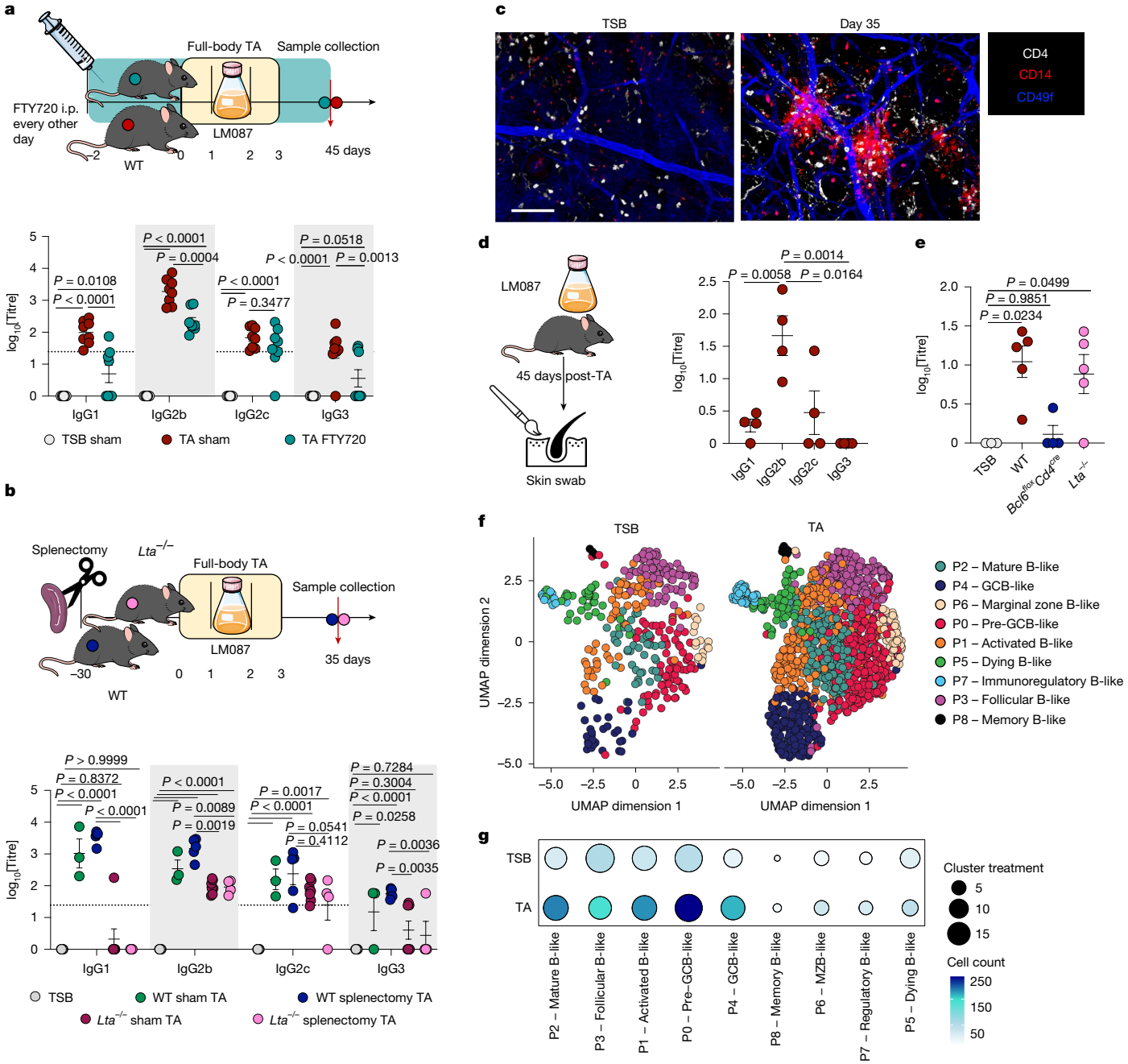

Fig. 4 | Skin secretes *S. epidermidis*-specific IgG2b and IgG2c antibodies independently of draining LN. a, Top: WT C57BL/6 mice were treated with or without (sham) FTY720 intraperitoneally (i.p.) 2 days before the TA with *S. epidermidis* LM087 and continuously every other day throughout the experiment, and samples were analysed 45 days post-TA as shown. Bottom: IgG1, IgG2b, IgG2c and IgG3 serum reactivity to *S. epidermidis* measured as $\log_{10}$ titres by ELISA; $n = 8$. **b**, Top: WT and *Lta*$^{-/-}$ mice underwent splenectomy or sham surgery 30 days before the TA, and samples were analysed 35 days later as shown. Bottom: IgG1, IgG2b, IgG2c and IgG3 serum reactivity to *S. epidermidis* measured as $\log_{10}$ titres by ELISA; $n = 5$ (TSB), 3 (WT sham TA), 5 (WT splenectomy TA), 7 (*Lta*$^{-/-}$ sham TA) and 4 (*Lta*$^{-/-}$ splenectomy TA). **c**, Ear dermis whole mount of a splenectomized *Lta*$^{-/-}$ unassociated (TSB) or associated (day 35) mouse, as shown in the scheme in **b** (CD4 (white), CD19 (red), CD49f (blue)), scale bar, 100 µm; observation confirmed in four mice. **d**,**e**, WT C57BL/6, *Bcl6*^{flox}*Cd4*^{cre} and *Lta*$^{-/-}$ mice were associated (TA) and skin swabs were analysed 45 days later, as shown in the scheme in **d** (left). **d**, Right: WT IgG isotypes in skin swabs reactive to *S. epidermidis* measured as $\log_{10}$ titres by ELISA; $n = 4$. **e**, Total IgG specific to *S. epidermidis* in skin swabs from WT ($n = 5$ TA, 3 TSB), *Lta*$^{-/-}$ ($n = 5$), and *Bcl6*^{flox} *CD4*^{cre} ($n = 4$) mice measured as $\log_{10}$ titres by ELISA. **f**,**g**, scRNA-seq from skin B cells of *Lta*$^{-/-}$ mice at baseline and 14 days post-TA; cells pooled from 5 mice (TA) and 3 mice (TSB). **f**, Uniform manifold approximation and projection (UMAP) representation of nine different B cell clusters. **g**, Normalized expansion profile of individual clusters between TSB and TA treatment. Results are representative of 2–3 independent experiments. All data are presented as mean values ± s.e.m., statistical significance was calculated by two-way ANOVA with Tukey's multiple comparison test (**a**,**b**), or ordinary one-way ANOVA with Tukey's multiple comparison test (**d**,**e**). The schematics in **a**,**b**,**d** were created using graphical templates from Servier Medical Art under a Creative Commons licence CC BY 4.0 (https://creativecommons.org/licenses/by/4.0/).

Antibody-mediated host protection

The presence of systemic antibody responses to bacteria may serve the purpose of preventing potential infections that result from barrier breaches, medical devices or immunosuppression[53]. It can also play the role of constraining the microbiota and reinforcing the symbiotic relationship of the host with its beneficial microorganisms. To test both possibilities, we first used a model of systemic infection with *S. epidermidis*

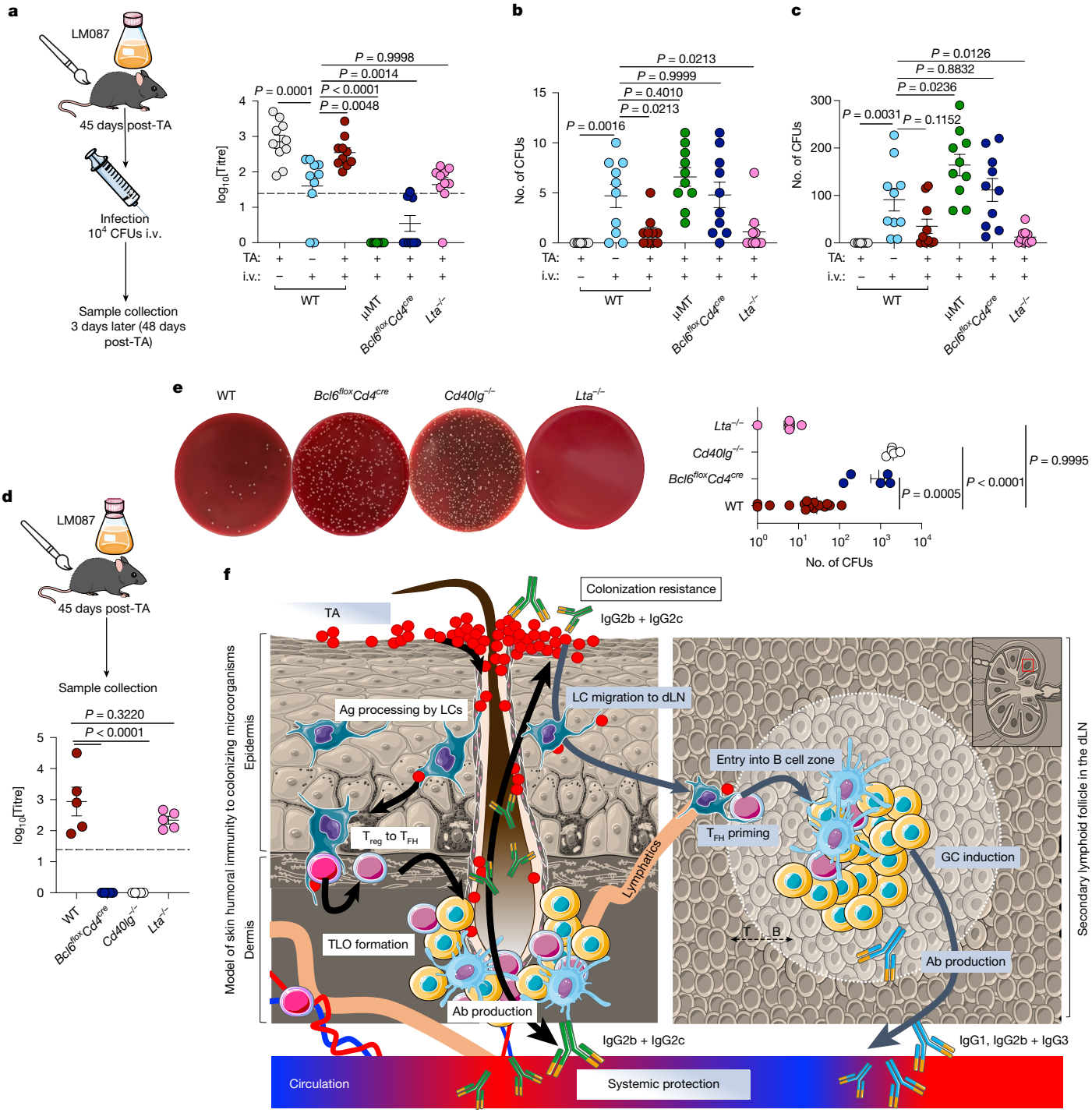

Fig. 5 | Commensal-specific antibodies provide systemic protection and control local skin bacterial burden. a–**c**, WT C57BL/6, μMT, *Bcl6*^{flox}*Cd4*^{cre} and *Lta*$^{-/-}$ mice were associated (TA) and 45 days later were infected intravenously (i.v.) with 10^4 CFUs *S. epidermidis*, and samples were analysed 3 days later as shown in the scheme in **a**; $n = 10$; positive control—naive WT infected; negative control—associated WT uninfected. **a**, Right: IgG serum reactivity to *S. epidermidis* measured as $\log_{10}$ titres by ELISA. **b**,**c**, Spleen-colonizing (**b**) and liver-colonizing (**c**) *S. epidermidis* CFUs enumerated per organ. **d**,**e**, WT C57BL/6, *Bcl6*^{flox}*Cd4*^{cre}, *Cd40lg*$^{-/-}$ and *Lta*$^{-/-}$ mice were associated (TA), and samples were analysed 45 days later as shown in the scheme in **d**. **d**, Bottom: IgG serum reactivity to *S. epidermidis* measured as $\log_{10}$ titres by ELISA; $n = 5$. **e**, Skin colonization burden was assessed as total CFUs per two ears; $n = 5$ (*Bcl6*^{flox}*Cd4*^{cre}, *Cd40lg*$^{-/-}$, *Lta*$^{-/-}$), 15 (WT) with representative Columbia agar plates containing *S. epidermidis* CFUs. **f**, Schematic representation of the proposed model. Skin-resident LCs may acquire commensals or commensal-derived antigens by reaching into the hair follicle. This initiates T_{reg} conversion into T_{FH} cells that migrate to the bases of the hair follicles in the dermis and form large GC-like TLOs with B cells. This further results in the topical release of IgG2b and IgG2c antibodies that control skin microbial colonization resistance and systemic secretion that ensures global host protection. Owing to cell migration, a parallel process is initiated in the skin-draining cLN, where, following TA with *S. epidermidis*, classical GCs are induced. These interactions provide a systemic IgG1, IgG2b and IgG3 response that is instrumental in systemic protection. Ag, antigen; Ab, antibody; dLN, draining LN. Results are representative of two independent experiments. All data are presented as mean values ± s.e.m.; statistical significance was calculated by ordinary one-way ANOVA with Dunnett's (**a**–**c**) or Tukey's (**d**,**e**) multiple comparison test. The schematics in **a**,**d**,**f** were created using graphical templates from Servier Medical Art under a Creative Commons licence CC BY 4.0 (https://creativecommons.org/licenses/by/4.0/).

in SPF mice that had previously been colonized with the same microorganism or not. At 45 days post-association, mice were intravenously infected with 10^4 colony-forming units (CFUs) of *S. epidermidis* (Fig. 5a). In unassociated mice, at 3 days post-systemic infection, bacteria were detected in various organs such as the spleen and liver (Fig. 5b,c). By contrast, mice previously associated with *S. epidermidis* had a significantly reduced bacterial burden in systemic tissues (Fig. 5b,c). The protection afforded by previous colonization was abrogated in mice deficient in B cell responses (μMT)[54] or mice deficient in T_{FH} cells (*Bcl6*^{flox}*Cd4*^{cre}; Fig. 5b,c), indicating that protective immunity was antibody-mediated. Of note, skin-restricted antibody production (in *Lta*$^{-/-}$ mice that lack secondary lymphoid organs) was sufficient to protect against systemic infection, highlighting the autonomous ability of the skin compartment to mount a protective antibody response (Fig. 5a–c). To further test this possibility, we performed a systemic challenge experiment in plasma cell-deficient (*Cd19*^{cre}*Prdm1*^{flox}) or AID-deficient (*Aicda*$^{-/-}$)[33] mice that had previously been associated with *S. epidermidis*. In both models and in contrast to control mice, mature class-switched and long-lived *S. epidermidis*-specific IgG antibodies were abrogated (Extended Data Fig. 9a). Further, antibody-deficient mice exhibited a higher infection burden in the spleen and liver compared to WT mice, supporting the idea that pre-existing humoral immunity, but not cellular immunity, is the determinant factor of host protection in the context of an infection with a symbiont (Extended Data Fig. 9b,c).

We next tested whether the same principle applied to local skin infection (Extended Data Fig. 9d). To this end, we associated mice with *S. epidermidis* and 40 days later infected them intradermally with the same microorganism. WT mice that had pre-existing humoral immunity were able to prevent bacterial translocation to skin-draining LNs. By contrast, μMT and *Cd19*^{cre}*Prdm1*^{flox} mice failed to control bacterial translocation post-intradermal infection comparably to previously unassociated mice (Extended Data Fig. 9d). Thus, skin colonization with commensals is sufficient to promote long-term protective humoral immunity, including skin autonomous antibody responses that play a non-redundant role in protection from infection caused by a symbiont.

We next examined whether colonization-induced antibodies could also contribute to colonization resistance. To this end, we topically associated WT, *Bcl6*^{flox}*Cd4*^{cre}, *Cd40lg*$^{-/-}$ and *Lta*$^{-/-}$ mice and 45 days later assessed IgG antibody titres and skin colonization burden (Fig. 5d,e). As we have previously shown, in WT mice, *S. epidermidis* established residence at a low level in the skin compartment (Fig. 5d,e and Extended Data Fig. 1a). By contrast, when mice were deficient in antibody production (*Bcl6*^{flox}*Cd4*^{cre} and *Cd40lg*$^{-/-}$), bacterial biomass was significantly higher, revealing a role for antibodies in the control of commensal burden at the skin surface (Fig. 5d,e). Of note, *Lta*$^{-/-}$ mice, which lack lymphoid structures and as such could produce antibodies only in the skin, controlled microbiota burden in a comparable manner to WT mice, indicating that locally formed IgGs were sufficient to convey microbial colonization resistance (Fig. 5e). We then tested whether, in the absence of B cell responses (*Bcl6*^{flox}*Cd4*^{cre} and *Cd40lg*$^{-/-}$ mice), tissue injury could be associated with enhanced bacterial translocation (Extended Data Fig. 9e). To this end, we performed punch biopsies before reassociation with *S. epidermidis* and assessed microbial load in the regional LN. At 3 days post-injury, mice lacking humoral immunity—*Bcl6*^{flox}*Cd4*^{cre} and *Cd40lg*$^{-/-}$ mice—had detectable microbial translocation, in contrast to the observations for WT control mice (Extended Data Fig. 9e). Collectively, our observations illustrate that skin autonomous production of IgG2b and IgG2c in the absence of professional lymphoid organs regulates host–microbiota interactions in the skin compartment and provides efficient protection from subsequent infections.

Here we propose a model of induction of *S. epidermidis*-specific immunoglobulins that is mediated by the uptake of bacterial antigens by LCs and induction of systemic and local B cell responses through classical LN- and tissue-induced GCs (Fig. 5f). Skin autonomous production of antibodies ensures stable colonization of the microbiota at low biomass through the topical release of microorganism-specific IgG2b and IgG2c antibodies. Both local and systemic antibody responses also provide systemic protection against possible subsequent infection (Fig. 5f). Collectively, these results reveal a compartmentalization of humoral immunity between lymphoid compartments and the skin.

Discussion

In contrast to the known development of TLOs at sites of chronic inflammation[55], microbiota-induced dermal GC-like structures are formed at homeostasis and support distinct isotypes from those generated in LNs. Mouse IgG2b and IgG2c are more effective at activating the complement pathway and binding to cellular Fc receptors than IgG1 (refs. 56,57). As such, in the skin, these isotypes provide a first line of protection with broad-spectrum effector functions. How the local tissue environment, including the known enrichment of transforming growth factor-β, contributes to the specification of these isotypes remains to be addressed[58].

Our work proposes that skin GC-like reactions may derive, at least in part, from the ability of T_{reg} cells to convert into T_{FH} cells. This specific interconversion is not seen in the context of strong stimuli vaccination[59] and may therefore be restricted to host–microbiota interactions[22]. Previous work revealed that tissue T_{reg} cells have distinct transcriptome and clonally expanded TCR repertoires[60]. As such, we could speculate that the skin T_{reg} repertoire may be biased towards canonical microbial specificities, a feature allowing for immune cell priming in the skin tissue itself. Indeed, observations of a preserved humoral response in LN-deficient *Lta*$^{-/-}$ mice strongly suggest local priming. Further, the skin-unique lymphocyte repertoire in the WT model provides another layer of evidence. In comparison to known kinetics of vaccination models[59], the initiation of immune response to skin colonization is delayed. This first response coincides with stepwise TLO formation through gradual lymphocyte concentration in the skin that eventually allows for antigen-specific priming (Extended Data Fig. 5c). The response is under strict control of LCs. It is therefore possible that LC-mediated priming could occur separately in the skin and draining LNs in a parallel manner; however, more focused study is required to further address this point in detail. Collectively, the findings of our work uncover a new concept of skin immune autonomy, revealing a previously unappreciated role for skin B cells in the control of host microbiota dialogue at large.

Online content

Any methods, additional references, Nature Portfolio reporting summaries, source data, extended data, supplementary information, acknowledgements, peer review information; details of author contributions and competing interests; and statements of data and code availability are available at https://doi.org/10.1038/s41586-024-08376-y.

1. Belkaid, Y. & Segre, J. A. Dialogue between skin microbiota and immunity. *Science* **346**, 954–959 (2014).
2. Cogen, A. L. et al. Skin microbiota: a source of disease or defence? *Br. J. Dermatol.* **158**, 442–455 (2008).
3. Naik, S. et al. Commensal-dendritic-cell interaction specifies a unique protective skin immune signature. *Nature* **520**, 104–108 (2015).
4. Linehan, J. L. et al. Non-classical immunity controls microbiota impact on skin immunity and tissue repair. *Cell* **172**, 784–796 (2018).
5. Enamorado, M. et al. Immunity to the microbiota promotes sensory neuron regeneration. *Cell.* **186**, 607–620 (2023).
6. Lehman, H. Skin manifestations of primary immune deficiency. *Clin. Rev. Allergy Immunol.* **46**, 112–119 (2014).
7. Meyer, T. C. et al. A comprehensive view on the human antibody repertoire against *Staphylococcus aureus* antigens in the general population. *Front. Immunol.* **12**, 651619 (2021).
8. Puhvel, S. M. et al. Levels of antibody to *Staphylococcus* epidermidis in patients with acne vulgaris. *Arch. Dermatol.* **92**, 88–90 (1965).
9. Metze, D. et al. Immunoglobulins coat microorganisms of skin surface: a comparative immunohistochemical and ultrastructural study of cutaneous and oral microbial symbionts. *J. Invest. Dermatol.* **96**, 439–445 (1991).

10. Debes, G. F. & McGettigan, S. E. Skin-associated B cells in health and inflammation. *J. Immunol.* **202**, 1659–1666 (2019).
11. Saul, L. et al. IgG subclass switching and clonal expansion in cutaneous melanoma and normal skin. *Sci. Rep.* **6**, 29736 (2016).
12. Conlan, S. et al. *Staphylococcus epidermidis* pan-genome sequence analysis reveals diversity of skin commensal and hospital infection-associated isolates. *Genome Biol.* **13**, R64 (2012).
13. Scharschmidt, T. C. et al. A wave of regulatory T cells into neonatal skin mediates tolerance to commensal microbes. *Immunity* **43**, 1011–1021 (2015).
14. Fagarasan, S. et al. Adaptive immune regulation in the gut: T cell–dependent and T cell–independent IgA synthesis. *Annu. Rev. Immunol.* **28**, 243–273 (2010).
15. Crotty, S. A brief history of T cell help to B cells. *Nat. Rev. Immunol.* **15**, 185–189 (2015).
16. Yu, D. et al. The transcriptional repressor Bcl-6 directs T follicular helper cell lineage commitment. *Immunity* **31**, 457–468 (2009).
17. Nurieva, R. I. et al. Bcl6 mediates the development of T follicular helper cells. *Science* **325**, 1001–1005 (2009).
18. Chung, Y. et al. Follicular regulatory T (Tfr) cells with dual Foxp3 and Bcl6 expression suppress germinal center reactions. *Nat. Med.* **17**, 983–988 (2011).
19. Nagase, N. et al. Isolation and species distribution of staphylococci from animal and human skin. *J. Vet. Med. Sci.* **64**, 245–250 (2002).
20. Belkaid, Y. et al. $CD4^+CD25^+$ regulatory T cells control *Leishmania major* persistence and immunity. *Nature* **420**, 502–507 (2002).
21. Cong, Y. et al. A dominant, coordinated T regulatory cell-IgA response to the intestinal microbiota. *Proc. Natl Acad. Sci. USA* **106**, 19256–19261 (2009).
22. Tsuji, M. et al. Preferential generation of follicular B helper T cells from Foxp3+ T cells in gut Peyer's patches. *Science* **323**, 1488–1492 (2009).
23. Rubtsov, Y. P. et al. Stability of the regulatory T cell lineage in vivo. *Science* **329**, 1667–1671 (2010).
24. Gribonika, I. et al. Class-switch recombination to IgA in the Peyer's patches requires natural thymus-derived Tregs and appears to be antigen independent. *Mucosal Immunol.* **12**, 1268–1279 (2019).
25. Hou, S. et al. FoxP3 and Ezh2 regulate Tfr cell suppressive function and transcriptional program. *J. Exp. Med.* **216**, 605–620 (2019).
26. Aloulou, M. et al. Follicular regulatory T cells can be specific for the immunizing antigen and derive from naive T cells. *Nat. Commun.* **7**, 10579 (2016).
27. Wang, J. Y. et al. Primary cutaneous follicular helper T-cell lymphoma: a case series and review of the literature. *Am. J. Dermatopathol.* **39**, 374–383 (2017).
28. Lowe, M. M. et al. Tertiary lymphoid structures sustain cutaneous B cell activity in hidradenitis suppurativa. *JCI Insight* **9**, e169870 (2024).
29. Lima, M. Cutaneous primary B-cell lymphomas: from diagnosis to treatment. *An. Bras. Dermatol.* **90**, 687–706 (2015).
30. Kitano, M. et al. Bcl6 protein expression shapes pre-germinal center B cell dynamics and follicular helper T cell heterogeneity. *Immunity* **34**, 961–972 (2011).
31. Cattoretti, G. et al. BCL-6 protein is expressed in germinal-center B cells. *Blood* **86**, 45–53 (1995).
32. Wang, X. et al. Follicular dendritic cells help establish follicle identity and promote B cell retention in germinal centers. *J. Exp. Med.* **208**, 2497–2510 (2011).
33. Muramatsu, M. et al. Class switch recombination and hypermutation require activation-induced cytidine deaminase (AID), a potential RNA editing enzyme. *Cell* **102**, 553–563 (2000).
34. Crouch, E. E. et al. Regulation of AID expression in the immune response. *J. Exp. Med.* **204**, 1145–1156 (2007).
35. Le Gallou, S. et al. A splenic IgM memory subset with antibacterial specificities is sustained from persistent mucosal responses. *J. Exp. Med.* **215**, 2035–2053 (2018).
36. Natsuaki, Y. et al. Perivascular leukocyte clusters are essential for efficient activation of effector T cells in the skin. *Nat. Immunol.* **15**, 1064–1069 (2014).
37. Ruddle, N. H. Regulation, maintenance, and remodeling of high endothelial venules in homeostasis, inflammation, and cancer. *Curr. Opin. Physiol.* **36**, 100705 (2023).
38. Hemmerich, S. et al. Sulfation-dependent recognition of high endothelial venules (HEV)-ligands by L-selectin and MECA 79, and adhesion-blocking monoclonal antibody. *J. Exp. Med.* **180**, 2219–2226 (1994).
39. Chen, Y. E. et al. Skin microbiota–host interactions. *Nature* **553**, 427–436 (2018).
40. Gunn, M. D. et al. A B-cell-homing chemokine made in lymphoid follicles activates Burkitt's lymphoma receptor-1. *Nature* **391**, 799–803 (1998).
41. Legler, D. F. et al. B cell-attracting chemokine 1, a human CXC chemokine expressed in lymphoid tissues, selectively attracts B lymphocytes via BLR1/CXCR5. *J. Exp. Med.* **187**, 655–660 (1998).
42. Schuler, G. & Steinman, R. M. Murine epidermal Langerhans cells mature into potent immunostimulatory dendritic cells in vitro. *J. Exp. Med.* **161**, 526–546 (1985).
43. Pierre, P. et al. Developmental regulation of MHC class II transport in mouse dendritic cells. *Nature* **388**, 787–792 (1997).
44. Zimara, N. et al. Langerhans cells promote early germinal center formation in response to *Leishmania*-derived cutaneous antigens. *Eur. J. Immunol.* **44**, 2955–2967 (2014).
45. Yao, C. et al. Skin dendritic cells induce follicular helper T cells and protective humoral immune responses. *J Allergy Clin. Immunol.* **136**, 1387–1397 (2015).
46. Levin, C. et al. Critical role for skin-derived migratory DCs and Langerhans cells in T_{FH} and GC responses after intradermal immunization. *J. Invest. Dermatol.* **137**, 1905–1913 (2017).
47. Bobr, A. et al. Acute ablation of Langerhans cells enhances skin immune responses. *J. Immunol.* **185**, 4724–4728 (2010).
48. Snapper, C. M. & Mond, J. J. Towards a comprehensive view of immunoglobulin class switching. *Immunol. Today* **14**, 15–17 (1993).
49. Brinkmann, V. et al. Fingolimod (FTY720): discovery and development of an oral drug to treat multiple sclerosis. *Nat. Rev. Drug Discov.* **9**, 883–897 (2010).
50. Ohl, L. et al. CCR7 governs skin dendritic cell migration under inflammatory and steady-state conditions. *Immunity* **21**, 279–288 (2004).
51. Banks, T. A. et al. Lymphotoxin-alpha-deficient mice. Effects on secondary lymphoid organ development and humoral immune responsiveness. *J. Immunol.* **155**, 1685–1693 (1995).
52. Futardo, G. C. et al. TNFα-dependent development of lymphoid tissue in the absence of $RORγt^+$ lymphoid tissue inducer cells. *Mucosal Immunol.* **7**, 602–614 (2014).
53. Zeng, M. Y. et al. Gut microbiota-induced immunoglobulin G controls systemic infection by symbiotic bacteria and pathogens. *Immunity* **44**, 647–658 (2016).
54. Kitamura, D. et al. A B cell-deficient mouse by targeted disruption of the membrane exon of the immunoglobulin mu chain gene. *Nature* **350**, 423–426 (1991).
55. Bery, A. I. et al. Role of tertiary lymphoid organs in the regulation of immune responses in the periphery. *Cell Mol. Life Sci.* **79**, 359 (2022).
56. Neuberger, M. S. & Rakewsky, K. Activation of mouse complement by monoclonal mouse antibodies. *Eur. J. Immunol.* **11**, 1012–1016 (1981).
57. Nimmerjahn, F. & Ravetch, J. V. Divergent immunoglobulin g subclass activity through selective Fc receptor binding. *Science* **310**, 1510–1512 (2005).
58. Liarte, S. et al. Role of TGF-β in skin chronic wounds: a keratinocyte perspective. *Cells* **9**, 306 (2020).
59. Gribonika, I. et al. Peyer's patch TH17 cells are dispensable for gut IgA responses to oral immunization. *Sci. Immunol.* **7**, eabc5500 (2022).
60. Burzyn, D. et al. A special population of regulatory T cells potentiates muscle repair. *Cell.* **155**, 1282–1295 (2013).

Methods

Mice

Germ-free C57BL/6NTac mice were bred and maintained in the National Institute of Allergy and Infectious Diseases (NIAID) Microbiome Program gnotobiotic animal facility. C57BL/6 SPF mice were purchased from Taconic. C57BL/10SgSnAi-[KO]UMT (μMT), C57BL/6-[Tg]CD11c:EYFP (CD11c–YFP) and C57BL/6-[KO]CCR7 (*Ccr7*$^{-/-}$) mice were obtained through the NIAID-Taconic exchange programme. *Il21r*$^{-/-}$ mice were provided by W. Leonard (NHLBI/NIH), *Bcl6*^{flox}*Cd4*^{cre} mice were provided by P. Schwartzberg (NIAID/NIH), *Cd40lg*$^{-/-}$ mice were provided by J. Kovac (Clinical Center/NIH), *Lta*$^{-/-}$ mice were provided by V. Lazarevic (NCI/CCR/NIH), huLang-DTR mice were provided by D. Kaplan (University of Pittsburgh) and *Aicda*$^{-/-}$ mice[33] were provided by C. Mayer (NCI/NIH). *Cd19*^{cre} (jax number 006785), *Prdm1*^{flox} (jax number 008100), *Foxp3*$^{eGFP\text{-}Cre\text{-}ERT2}$ (jax number 016961), Rosa26^{tdTomato} (jax number 007909) and AID–GFP (jax number 018421) mice were purchased from Jackson Laboratories. BCL6–YFP mice were provided by D. Dominguez-Sola (Mount Sinai, NYC). All mice were bred and maintained under pathogen-free conditions at an American Association for the Accreditation of Laboratory Animal Care-accredited animal facility at the NIAID and housed following the procedures outlined in the Guide for the Care and Use of Laboratory Animals (temperature, from +20 to +24 °C; humidity, 30–70%; 14 h light/10 h dark). All experiments were performed at the NIAID under an animal study proposal (LHIM-3E) approved by the NIAID Animal Care and Use Committee. Sex- and age-matched mice between 6 and 12 weeks of age were used for each experiment. When possible, preliminary experiments were performed to determine requirements for sample size, considering resources available and ethical, reductionist animal use. Each mouse of the different experimental groups is reported (see *n* in figure legends). Exclusion criteria such as inadequate staining or low cell yield due to technical problems were predetermined. Animals were assigned randomly to experimental groups. Experiments were blinded when possible.

TA, infection, FTY720 treatment, LC depletion and TAM-inducible labelling

For TA with bacterial culture, TSB was inoculated at an optical density at 600 nm (OD_{600nm}) of 0.01 with a bacterial suspension prepared with fresh colonies and incubated for approximately 7 h at 37 °C until OD_{600nm} reached 0.8. For the TA with bacteria, each mouse was associated by placing 2.5 ml of the bacterial suspension (approximately 10^9 CFUs ml^{-1}) across the entire skin surface (approximately 36 cm^2) using a sterile cotton swab. The application of bacterial suspension was repeated every day for four days. For infection, mice were intravenously infected with 10^4 or intradermally infected with 10^6 CFUs of *S. epidermidis* NIHLM087. Bacteria were enumerated in the liver and spleen 3 days after intravenous infection or in skin-draining LN 5 days after intradermal infection by assessing CFUs using traditional bacteriology techniques. For FTY720 treatment, mice were injected with 1 mg kg^{-1} of fingolimod (Sigma) intraperitoneally every other day throughout the experiment. The control group received sham injections. For LC depletion, huLang-DTR mice were injected with 1 μg diphtheria toxin intraperitoneally 4 days before the TA. The control group received a sham injection. For TAM-inducible labelling, a *Foxp3*$^{eGFP\text{-}Cre\text{-}ERT2}$ female mouse was crossed with a Rosa26^{tdTomato} male mouse and F1 male mice at the age of 8–10 weeks were gavaged once with 10 mg TAM (Sigma) dissolved in corn oil 5 days before the association. FOXP3$^+$ T_{reg} labelling with tdTomato was persistent for at least 21 days after the association.

Splenectomy

Mice were anaesthetized with ketamine and xylazine, and an incision was made in the middle of the abdomen, moving aside the muscles and other tissues to reveal the spleen. The spleen was then removed, and the incision was closed. Mice were monitored for 30 days for full recovery before the onset of the experiments.

Tissue processing

Ears were excised and separated into the ventral and dorsal sheets. Tissue samples were digested in RPMI containing 55 μM β-mercaptoethanol, 20 μM HEPES (HyClone), 0.25 mg ml^{-1} Liberase purified enzyme blend (RocheDiagnostic) and 0.2 mg ml^{-1} DNase I (Sigma) and incubated for 1.5 h at 37 °C and 5% CO_2. Digested skin sheets were homogenized using the Medicon/Medimachine tissue homogenizer system (Becton Dickinson) and spun down at 500*g* for 5 min. Ear-draining LNs were collected and pushed through a 70-μm cell strainer. After being spun down at 500*g* for 5 min, the cell pellets were used for the assays. Bone marrow was flushed using cold PBS and processed through a 70-μm filter, and the cell pellet was lysed in ACK (ThermoFisher) lysis buffer for 5 min at room temperature. Cells were washed twice with PBS before the assays. Skin swabs were collected by swabbing each side of the ear sheet for 10 s with a sterile cotton swab prewetted in 300 μl of PBS. Samples were centrifuged for 10 min at 3,000*g*, and the resulting PBS solution was used for the ELISA.

Phenotypic analysis

Single-cell suspensions were stained with LIVE/DEAD Fixable Blue Dead Cell Stain Kit (Invitrogen) in PBS to exclude dead cells. For the detection of transcription factors, cells were stained using the FOXP3 staining set (ThermoFisher Scientific) according to the manufacturer's protocol. For detection of Langerin expression, cells were fixed and permeabilized with BD Cytofix/Cytoperm and stained in BD Perm Wash buffer (BD Biosciences). Cells were stained with the following antibodies: hamster anti-mouse TCRβ–BUV737 (H57-597, BD Horizon, catalogue number 612821, 1:400), rat anti-mouse IFNγ–BV421 (XMG1.2, BD Horizon, catalogue number 563376, 1:100), rat anti-mouse IL-4–PE (11B11, BioLegend, catalogue number 504103, 1:100), rat anti-mouse CD4–BV711 (GK1.5, BD Horizon, catalogue number 563050, 1:400), rat anti-mouse CD4–BV510 (RM4-5, BD Horizon, catalogue number 563106, 1:500), rat anti-mouse CD4–BV650 (RM4-5, BD Horizon, catalogue number 563747, 1:400), rat anti-mouse CD62L–BV605 (MEL-14, BD Horizon, catalogue number 563252, 1:600), rat anti-mouse CD62L–PE (MEL-14, BioLegend, catalogue number 104407, 1:500), rat anti-mouse CD45–BUV396 (30-F11, BD Horizon, catalogue number 564279, 1:300), rat anti-mouse CD45–BV650 (30-F11, BD Horizon, catalogue number 563410, 1:300), rat anti-mouse CD45–APC (30-F11, eBioscience, catalogue number 17-0451-82, 1:400), rat anti-mouse CD45–BV510 (30-F11, BD Horizon, catalogue number 563891, 1:400), rat anti-mouse CD24–BUV396 (M1/69, BD OptiBuild, catalogue number 744471, 1:200), rat anti-mouse CD24–BV605 (M1/69, BD Horizon, catalogue number 563060, 1:200), mouse anti-BCL6–AF488 (K112-91, BD Pharmingen, catalogue number 561524, 1:100), rat anti-mouse CXCR5–AF647 (L138D7, BioLegend, catalogue number 145531, 1:100), hamster anti-mouse PD-1–BV711 (J43, BD OptiBuild, catalogue number 744547, 1:200), rat anti-mouse PD-1–BV605 (29F.1A12, BioLegend, catalogue number 135219, 1:200), rat anti-mouse/human Ki-67-PE–Cy7 (SolA15, eBioscience (ThermoFisher Scientific), catalogue number 25-5698-82, 1:300), rat anti-mouse IgD–PerCP–Cy5.5 (11-26c.2a, BioLegend, catalogue number 405709, 1:800), rat anti-mouse IgD–BV605 (11-26c.2a, BioLegend, catalogue number 405727, 1:600), rat anti-mouse IgG1–BV711 (A85-1, BD Horizon, catalogue number 565786, 1:200), rat anti-mouse IgG2b–FITC (R12-3, BD Pharmingen, catalogue number 553395, 1:200), rat anti-mouse B220–PE-CF594 (RA3-6B2, BD Horizon, catalogue number 562313, 1:400), rat anti-mouse B220–APC–Cy7 (RA3-6B2, BD Horizon, catalogue number 552094, 1:400), rat anti-mouse CD19–BUV396 (1D3, BD Horizon, catalogue number 563557, 1:300), rat anti-mouse CD19–BV785 (6D5, BioLegend, catalogue number 115543, 1:300), rat anti-mouse/human GL-7–eF450 (GL-7, eBioscience (ThermoFisher Scientific), catalogue number 48-5902-82, 1:200), rat anti-mouse/human GL-7–PerCP–Cy5.5 (GL-7, BioLegend, catalogue number 144609, 1:200), rat anti-mouse CD38–APC (90, BioLegend,

catalogue number 102711, 1:300), hamster anti-mouse CD95–BV510 (Jo2, BD Horizon, catalogue number 563646, 1:300), rat anti-mouse/hamster/human FOXP3–AF700 (FJK-16s, eBioscience (ThermoFisher Scientific), catalogue number 56-5773-82, 1:100), rat anti-mouse FOXP3–PerCP–Cy5.5 (R16-715, BD Pharmingen, catalogue number 563902, 1:100), rat anti-mouse MHCII–AF700 (M5/114.15.2, eBioscience (ThermoFisher Scientific), catalogue number 56-5321-82, 1:200), rat anti-mouse CD11b–FITC (M1/70, eBioscience (ThermoFisher Scientific), catalogue number 11-0112-82, 1:200), hamster anti-mouse CD11c–PeCy7 (N418, BioLegend, catalogue number 117317, 1:200), rat anti-mouse Langerin (CD207)–PE (929F3.01, Dendritics, catalogue number DDX0362P-100, 1:200), rat anti-mouse CD44–BUV395 (IM7, BD OptiBuild, catalogue number 740215, 1:400), rat anti-mouse CD44–PE–Cy7 (IM7, BD Pharmingen, catalogue number 560569, 1:400), rat anti-mouse CD103–BV510 (M290, BD Horizon, catalogue number 563087, 1:200), mouse anti-mouse/rat XCR1–APC (ZET, BioLegend, catalogue number 148205, 1:200), rat anti-mouse F4/80–APC–Cy7 (BM8, BioLegend, catalogue number 123117, 1:200) and rat anti-mouse CD25–Per-CP–Cy5.5 (PC61.5, eBioscience (ThermoFisher Scientific), catalogue number 45-0251-82, 1:200). Staining was performed in the presence of FcBlock (ThermoFisher), 0.2 mg ml^{-1} purified rat IgG, and 1 mg ml^{-1} of normal mouse serum (Jackson Immunoresearch). Cells were acquired on a BD LSRFortessa cell analyser (BD Biosciences) equipped with FACSDiva software (v9.0) and analysed using FlowJo software (v10.8.2).

Confocal microscopy of ear dermis whole-mount and LN tissue sections

For ear dermis whole mount, ear pinnae were split with forceps, fixed in 1% paraformaldehyde solution (Electron Microscopy Sciences) overnight at 4 °C and blocked in 1% BSA, 0.25% Triton X blocking buffer for 2 h at room temperature. For LN sections, LNs were collected and fixed at 10 mg ml^{-1} paraformaldehyde for 24 h. Samples were washed in phosphate buffer and dehydrated in 30% sucrose phosphate buffer, mounted in O.C.T. Compound (Fisher) and snap-frozen on dry ice. Sections with 11 µm thickness were cut on a cryostat. Sections were washed in phosphate buffer and blocked in 1% BSA, 0.25% Triton X blocking buffer for 30 min at room temperature. Tissues were stained overnight at 4 °C in blocking buffer with antibodies: rat anti-mouse CD19–APC (1D3, BD Pharmingen, catalogue number 561738, 1:200), rat anti-mouse CD49f–eF450 (eBioGoH3, eBioscience (ThermoFisher Scientific), catalogue number 48-0495-82, 1:200), rat anti-mouse CD45-AF700 (30-F11, eBioscience (ThermoFisher Scientific), catalogue number 56-0451-82, 1:200), rat anti-mouse CD4–eF570 (RM4-5, eBioscience (ThermoFisher Scientific), catalogue number 41-0042-82, 1:200), rat anti-mouse CD4–AF700 (GK1.5, eBioscience (ThermoScientific), catalogue number 56-0041-82, 1:200), rat anti-mouse CD35–BV510 (8C12, BD OptiBuild, catalogue number 740132, 1:500), rat anti-mouse CXCR5–AF647 (L138D7, BioLegend, catalogue number 145531, 1:100), hamster anti-mouse PD-1–BV421 (J43, BD Horizon, catalogue number 562584, 1:200), rat anti-mouse HEV–AF488 (MECA-79, eBioscience, catalogue number 53-6036-82, 1:200), rat anti-mouse LYVE-1–eF615 (ALY7, eBioscience, catalogue number 42-0443-82, 1:200), rat anti-mouse CXCL13–APC (DS8CX13, eBioscience, catalogue number 17-7981-82, 1:200), rat anti-mouse IgG2b–FITC (R12-3, BD Pharmingen, catalogue number 553395, 1:200), rat anti-mouse IgD–PE (11-26c.2a, BD Pharmingen, catalogue number 558597, 1:600), rat anti mouse B220-eF615 (RA3-6B2, eBioscience (ThermoScientific), catalogue number 42-0452-82, 1:400), rat anti-mouse Langerin (CD207)–AF488 (929F3.01, Dendritics, catalogue number DDX0362A488-100, 1:200) . After being washed three times with PBS, tissues were mounted with ProLong Gold (Molecular Probes) antifade reagent. Ear pinnae and LN section images were captured on a Leica TCS SP8 confocal microscope equipped with LAS X software. Images were analysed using Imaris Bitplane software (v10.0).

ELISA and Elispot

For the ELISA, mice were bled at euthanization, and serum and ear skin swab samples were analysed individually in flat-bottom 96-well MaxiSorp microtitre plates (Nunc). Wells were coated with heat-killed bacterial culture in PBS (approximately 10 µg ml^{-1}) overnight in PBS at 4 °C. The plates were washed in PBS and blocked with 0.1% bovine serum albumin (BSA) in PBS, and the samples were then serially diluted in 0.1% BSA in PBS, and aliquots were added to corresponding sub-wells. The plates were kept at 4 °C overnight, and after washing in PBS, the plates were incubated with alkaline phosphatase (AP)-conjugated isotype-specific goat anti-mouse antibodies (SouthernBiotech): goat anti-mouse IgG1–AP (catalogue number 1071-04, 1:1,000), goat anti-mouse IgA–AP (catalogue number 1040-04, 1:1,000), goat anti-mouse IgM–-AP (catalogue number 1021-04, 1:1,000), goat anti-mouse IgG–AP (catalogue number 1036-04, 1:1,000), goat anti-mouse IgG2b–AP (catalogue number 1091-04, 1:1,000), goat anti-mouse IgG2c–AP (catalogue number 1079-04, 1:1,000), goat anti-mouse IgG3–AP (catalogue number 1100-04, 1:1,000), goat anti-mouse IgE–AP (catalogue number 1110-04, 1:1,000). Plates were washed, and the phosphatase substrate, *p*-nitrophenyl phosphatase (Sigma-Aldrich), was added to each well. The reaction was read at 405 nm using a BioTek Synergy H1 microplate reader supplied with Gen5 3.14 software. The antibody titres were defined as the interpolated dilutions of the samples, giving rise to an absorbance on the linear part of the curve 0.4 above the background. For the Elispot assay, Elispot 96-well plates (MultiScreen HTS, Millipore) were coated with heat-killed *S. epidermidis* culture in PBS (10 µg ml^{-1}). After blocking with 0.1% BSA in PBS, duplicate wells were incubated with mononuclear cells from the femur bone marrow or skin. The cells were incubated for 5 h at 37 °C and 5% CO_2. After the cells were thoroughly washed in PBS with 0.05% Tween 20, AP-conjugated goat anti-mouse antibodies (SouthernBiotech) in 100 µl per well were added. The bound antibodies marking single-antibody-producing cells were visualized by adding 50 µl per well of Sigmafast BCIP/NBT B5655 1 tablet per 10 ml deionized water (Sigma-Aldrich). Spot-forming cells were counted using an ImmunoSpot analyser (CTL) with CTL Switchboard 2.6.1.

scRNA-seq

Cells were isolated from the skin. After staining on ice with surface markers that distinguish B cells and $CD4^+$ T cells and TotalSeqC hashtag antibodies (BioLegend) to label each sample uniquely, cells were washed and sorted on the basis of binding to the labelled antibodies on a FACSAria Fusion cell sorter (BD Biosciences) using the 85-µm nozzle. All samples were pooled together, and cells were loaded on a Chromium chip (10X Genomics). A total of 15,000 cells were loaded for B cells in 1 lane, whereas for T cells, 30,000 cells were loaded per lane for a total of 4 lanes. Libraries for gene expression, hashtag markers and BCRs or TCRs were then prepared using a Chromium Single Cell 5′ Reagent kits following the manufacturer's instructions. Libraries were sequenced on a NextSeq 1000 (for T cells) and NextSeq 2000 (for B cells) platform (Illumina). Illumina files were converted to FASTQ files using bcl-output command v3.10.5, and data were filtered and mapped to mm10 reference genome (https://cf.10xgenomics.com/supp/cell-exp/refdata-gex-mm10-2020-A.tar.gz) by using Cell Ranger v7.1.0 (10X Genomics).

scRNA-seq for T cells. The overall sequencing quality was high for the four T cell mRNA libraries for which >95% of bases in the barcode and unique molecular identifier (UMI) regions had Q30 quality score or above, and >89% of bases in the RNA reads had Q30 or above. Furthermore, the median gene count range was 1,364–1,500 along with a sequencing saturation of >71% and about 70% of the reads mapped confidently to the transcriptome. The mean read count per cell was about 30,000 across the 4 samples. For the four TCR libraries, the percentage of cells with productive V–J spanning (TRA, TRB) pairs was >80%, and the mean read count per cell was across 18,000. For the four

HTO libraries, mean read count per cells was between 1,600 and 2,500 with >93% of valid barcodes.

In the downstream analysis of the expression data, the cellranger output (filtered_feature_bc_matrix) was loaded into Seurat (v5.0.2)[61] using the CreateSeuratObject function, which retained the genes detected in at least 3 cells with at least 200 genes detected per cell (min.cells = 3 and min.features = 200). Cells with 200–3,000 RNAs, less than 5% of mitochondrial RNA and less than 10,000 RNA reads were kept for further analysis. Hashtag libraries were demultiplexed using a two-step procedure. First, all hashtags from one tissue were combined and demultiplexed using Seurat's HTODemux. For a more detailed sample view, data were demultiplexed for each hashtag using MULTIseqDemux[62]. Data were then processed utilizing 17 PCs for neighbour finding and a resolution of 0.8 for cluster identification by a two-step process for removing outlier clusters that represented contaminants. In the first step, outlier clusters 7 and 13 were filtered out, whereas the second step led to the removal of outlier cluster 18. The remaining clusters were then annotated manually using differentially expressed genes between Seurat clusters using default parameters. TCR data were processed using scRepertoire v.2.0.0 (ref. 63) utilizing the amino acid (CDR3) clonotype definition and added as metadata to the Seurat object. Per cluster and per tissue clonotype abundance was extracted from the Seurat object and clonotype overlap between clusters in the skin was visualized using the circlize (v.0.4.15) package[64]. Individual sequences are plotted on the circos graph (denoted by the axis numbers). For each cluster, the sequences are organized by clonotypes, and clonotypes are ordered by their abundance values. Each link in the circos plot represents a clonotype, which appears in both linked clusters, with the width of the link at each end representing the clonotype abundance in that cluster. For overlap analysis between the tissues, the percentage of TCRs detected in the skin that were also detected in the spleen, LNs or both was calculated for each mouse.

scRNA-seq for B cells. The overall sequencing quality was high for the B cell mRNA library with >94% of bases in the barcode, and UMI regions had Q30 quality score or above, and >94% of bases in the RNA reads had Q30 or above. Furthermore, the median gene count range was 946 along with a sequencing saturation of >42%, and about 81% of the reads mapped confidently to the transcriptome. The mean read count per cell was about 23,000. For the HTO library, mean read count per cells was 428 with >97% of valid barcodes.

In the downstream analysis of the B cell expression data, the Cell Ranger output (filtered_feature_bc_matrix.h5 file) was loaded into Seurat version 3.1/4.1.0 (ref. 61) using the CreateSeuratObject that retained the genes detected in at least 100 cells with at least 200 genes detected per cell (min.cells = 100 and min.features = 200). For filtering out the low-quality cells, we used the isOutlier function of the R package scuttle (v1.4.0) with nmads (number of median absolute deviations) thresholds of 4 for highest allowed mitochondrial content (percent.mt), and 3 and 2.5 for the lowest and highest gene and UMI counts (nFeature_RNA and nCount_RNA) allowed, respectively. log-normalization (LogNormalize) of the RNA count data and centred log ratio transformation of the HTO count data were carried out using the NormalizeData function. For HTO demultiplexing the cells into the TSB and TA treatment groups and removing any additional doublets, HTODemux was run with positive.quantile = 0.99, whereas FindIntegrationAnchors, IntegrateData, RunPCA, RunUMAP and FindNeighbors functions of Seurat were run with the top 20 dimensions. The FindClusters function of Seurat was used to cluster the cells with the default Louvain clustering setting and a resolution of 0.8. Clusters were annotated manually using differentially expressed genes between Seurat clusters using default parameters.

Bulk BCR-seq

High-throughput sequencing of the adaptome in the study samples was conducted using the iR-RepSeq+ service provided by iRepertoire. Next-generation sequencing libraries were generated for each of the 12 samples in replicate, encompassing the BCR heavy chain, with coverage and distinction of IgM, IgD, IgE, IgA, IgG1, IgG2 (IgG2a, IgG2b and IgG2c) and IgG3 subtypes. This technology facilitates amplification of the BCR heavy chain while addressing known sources of errors in AIRR-seq analyses[65]. The sequencing protocol involves the initial utilization of primer pairs for each V–D–J combination, enabling extension with tags for subsequent global amplification of the heavy chains. This amplification process is conducted in a single assay, incorporating UMIs during the reverse transcription step to distinguish between individual RNA molecules and minimize the impact of PCR duplicates and sequencing errors.

Reverse transcription was performed using Qiagen OneStep RT-PCR mix, followed by selection of first- strand cDNA and removal of remnant primers using SPRIselect bead selection (Beckman Coulter). Subsequently, a second round of binding and extension was carried out with a V gene primer mix, and SPRIselect beads were used to purify the first- and second-strand synthesis products. Library amplification was achieved using primers specific to communal sites engineered onto the 5′ end of the C and V primers used in the initial synthesis steps. The final constructed library includes Illumina dual index sequencing adaptors, a 10-nucleotide UMI, and an 8-nucleotide internal barcode associated with the C gene primer. Amplified libraries were multiplexed and pooled for sequencing on the Illumina NextSeq 1000 platform with one P1 600-cycle kit (300 paired-end reads) at iRepertoire. The resulting immune receptor sequence data cover the second framework region through the beginning of the constant region, including the CDR3 hypervariable region. Sequencing raw data were analysed using the iRmap v3.0 software[66–68]. Briefly, the sequenced reads were demultiplexed according to the Illumina dual indices and barcode sequences. Merged reads were mapped to germline V, D, J and C reference sequences using the IMGT reference library (https://www.imgt.org). CDR3 regions defined by mapping results were translated into amino acids. The dataset was then condensed by combining UMIs and CDR3 regions to remove incorrect CDR3s introduced by sequencing and amplification. Reads with the same combination of CDR3 and UMI were condensed into one UMI count.

For BCR clonotype overlap analysis between tissues and D50 calculations, clonotypes were defined as the combination of a unique CDR3 amino acid sequence and a specific heavy chain V segment. For the mutated BCR overlap analysis, clonotypes were defined as the combination of a unique CDR3 amino acid sequence, a specific heavy chain V segment, and a specific number of mutations (across the entire V segment, 'v_mismatches'). For overlap analysis between the tissues, the percentage of BCRs detected in the skin, while also being detected in the spleen, LNs or both, was calculated for each mouse. The D50 diversity index was calculated as the percentage of the unique clonotypes (ordered by descending abundance) representing half of the total BCR repertoire volume.

Statistics and software

Statistical analysis was performed using GraphPad Prism9. No statistical methods were used to determine the sample size. Data are presented as mean ± s.e.m. using one-way or two-way ANOVA with Dunnett's, Šidák's or Tukey's multiple comparison test or two-tailed unpaired *t*-test, or two-tailed Mann–Whitney test, as stated in each figure legend. All graphs were plotted using Prism (v9) and edited for appearance using Adobe Illustrator (v28.0) or MS Powerpoint (v16.79.1). For antibody titres, statistical analysis was performed on the log-transformed data.

Reporting summary

Further information on research design is available in the Nature Portfolio Reporting Summary linked to this article.

Data availability

scRNA-seq data and Seurat objects for B cells are available under the Gene Expression Omnibus (GEO) accession number GSE250572, scRNA-seq data and Seurat objects for T cells are available under GEO accession number GSE272390, and bulk BCR-seq data and processed chain data are available under GEO accession number GSE279095. All BCR clonotype sequences are summarized as Supplementary Table 2, and all BCR clonotype sequences with somatic hypermutation are summarized as Supplementary Table 3 (available via Zenodo at https://zenodo.org/records/13987214 (ref. 69). Source data are provided with this paper.

Code availability

All code used in the analysis of sequencing data (including scRNA-seq and bulk BCR-seq post-processing by iRepertoire) is available via GitHub at https://github.com/Eduard278/Gribonika_et_al_2024.

61. Hao, Y. et al. Dictionary learning for integrative, multimodal and scalable single-cell analysis. *Nat. Biotechnol.* **42**, 293–304 (2024).
62. McGinnis, C. S. et al. MULTI-seq: sample multiplexing for single-cell RNA sequencing using lipid-tagged indices. *Nat. Methods* **16**, 619–626 (2019).
63. Brocherding, N. et al. scRepertoire: an R-based toolkit for single-cell immune receptor analysis. *F1000Res* **9**, 47 (2020).
64. Gu, Z. et al. circlize implements and enhances circular visualization in R. *Bioinformatics*. **30**, 2811–2812 (2014).
65. Beechem, J. M. High-plex spatially resolved RNA and protein detection using digital spatial profiling: a technology designed for immuno-oncology biomarker discovery and translational research. *Methods Mol. Biol.* **2055**, 563–583 (2020).
66. Han, J. & Lotze, M. T. The adaptome as a biomarker for assessing cancer immunity and immunotherapy. *Methods Mol. Biol.* **2055**, 369–397 (2020).
67. Liu, H. et al. The methods and advances of adaptive immune receptors repertoire sequencing. *Theranostics* **11**, 8945–8963 (2021).
68. Wu, S. G. et al. High throughput sequencing of T-cell receptor repertoire using dry blood spots. *J. Transl. Med.* **17**, 47 (2019).
69. Gribonika, I., Ansaldo, E. & Link, V. Skin autonomous antibody production regulates host-microbiota interactions. *Zenodo* https://zenodo.org/records/13987214 (2024).

Acknowledgements This study was supported by the Division of Intramural Research of the NIAID (Y.B., I.G., L.C., V.I.B., V.M.L., E.A., P.J.P.-C.), R01 AI175642 (M.A.F.), the Chan Zuckerberg Biohub (M.A.F.) and the Bill and Melinda Gates Foundation (M.A.F. and Y.B.). L.C. was supported by the Cancer Research Institute Irvington Fellowship programme. D.B. was supported by an Early Postdoc Mobility Fellowship and a Postdoc fellowship from the Swiss National Science Foundation. We thank all Belkaid laboratory members, especially P. W. Kulalert, N. Bouladoux and A. Wells for scientific input, resource sharing and editorial comments; V. Lazarevic and C. Spinner for providing *Lta*$^{-/-}$ mice, W. Leonard and R. Spolski for providing *Il21r*$^{-/-}$ mice, J. Kovac for providing *Cd40lg*$^{-/-}$ mice, P. Schwartzberg for providing *Bcl6*^{flox}*Cd4*^{cre} mice and C. Mayer for providing *Aicda*$^{-/-}$ mice; the NIAID animal facility staff for care of all animals involved in the study; O. Schwartz, J. Kabat, M. Smelkinson and the NIAID Biological Imaging facility for providing equipment and technical support in confocal microscopy; I. Douagi and the NIAID Flow Cytometry Unit for cell sorting assistance; G. Koroleva for sequencing assistance; J. Lack, N. Yoon and the NIAID Bioinformatics Unit for sample preparation post-sequencing; and R. Germain, T. Veres and P. Schwartzberg (NIH NIAID) for protocol exchanges and discussions. Schematic parts of the figures were drawn in MS PowerPoint using graphical templates from Servier Medical Art (https://smart.servier.com). Servier Medical Art by Servier is licensed under a Creative Commons Attribution 4.0 unported licence (https://creativecommons.org/licenses/by/4.0/).

Author contributions I.G. and Y.B. designed the concept of the study and wrote the original manuscript. I.G. planned and performed all experiments, analysed data and created the figures. L.C. and I.G. ran the initial pilot experiment and performed long-term kinetics experiments. V.I.B. and I.G. performed experiments concerning functional phenotype. P.J.P.-C. prepared and maintained all bacterial cultures used throughout the study. I.G., V.M.L. and E.A. planned the sequencing experiments; I.G. and V.I.B. prepared samples for sequencing; V.M.L., E.A. and C.O. handled all sequencing data; V.M.L. analysed and visualized scRNA-seq B cell and CD4^{+} T cell data. E.A. analysed and visualized TCR clonal sharing and performed analysis on bulk BCR-seq post initial analysis by iRepertoire. C.O. performed quality control and prepared raw scRNA-seq data for downstream applications. D.B. and M.A.F. participated in project progress meetings and exchanged assay protocols. Y.B. performed project administration. All of the authors reviewed and contributed to editing the manuscript before submission.

Competing interests M.A.F. is a co-founder of Kelonia and Revolution Medicines, a member of the scientific advisory boards of the Chan Zuckerberg Initiative, NGM Biopharmaceuticals and TCG Labs–Soleil Labs, and an innovation partner at The Column Group. D.B., Y.B. and M.A.F. are inventors on patent applications submitted by Stanford University and the Chan Zuckerberg Biohub that cover methods for using engineered bacteria to elicit antigen-specific immune cells.

Additional information

Supplementary information The online version contains supplementary material available at https://doi.org/10.1038/s41586-024-08376-y.

Correspondence and requests for materials should be addressed to Inta Gribonika or Yasmine Belkaid.

Peer review information *Nature* thanks Kenji Kabashima and the other, anonymous, reviewer(s) for their contribution to the peer review of this work.

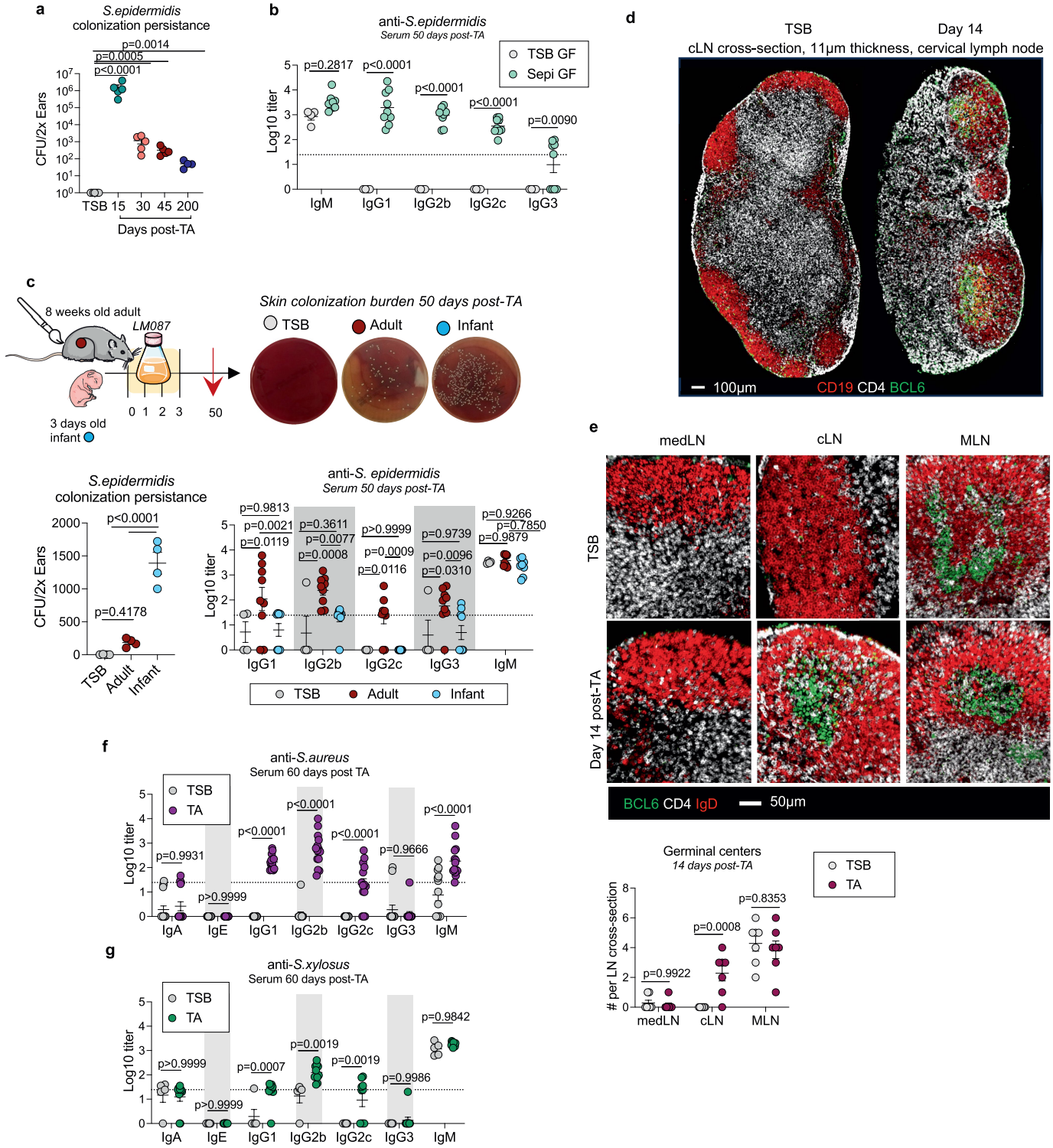

Extended Data Fig. 1 | See next page for caption.

Extended Data Fig. 1 | Topical association induces long-lasting skin colonization and humoral response. a, Enumeration of the total count of *S. epidermidis* colony forming units (CFU) per 2 ears per mouse 15, 30, 45, and 200 days after the association; n = 9 (TSB), 5 (Day 15-45), 4 (Day 200). Results are representative of 2 independent experiments. **b**, C57BL/6 Germ-free (GF) mice topically associated with S.*epidermidis* LM087 and 50 days later serum antibody titres assessed by ELISA assay as shown in the scheme; n = 4 (TSB), 9 (TA). **c**, Adult mice (8 weeks old) or infant pups (3 days old) were simultaneously associated with *S.epidermidis* as shown in the scheme and 50 days later skin colonization burden (n = 4) and serum antibody titres assessed, n = 3 (TSB), 9 (TA). **d**, Germinal centre formation ($Bcl6^+$ area in green) in skin-draining cervical lymph-node (cLN) 14 days post-TA compared to unassociated (TSB) Bcl6-YFP reporter mouse as shown by confocal microscopy, observation confirmed in over 20 mice; cryosection thickness 11 µm; scale: 100 µm. **e**, Representative confocal images of germinal centre formation ($Bcl6^+$ area in green) in B cell follicle (IgD^+ area in red; surrounding T cell zone in white) and enumeration of total GCs of mediastinal LN (medLN), skin-draining cervical lymph-node (cLN) or mesenteric LN (MLN) 14 days post-TA compared to unassociated (TSB) in Bcl6-YFP reporter mice; n = 7; cryosection thickness 11 µm; scale: 50 µm. **f**,**g**, Specific pathogen-free (SPF) C57BL/6 mice topically associated (TA) with *Staphylococcus aureus*, n = 14 (**f**) or *Staphylococcus xylosus*, n = 10 (TA; TSB = 5) (**g**) in Tryptic Soy Broth (TSB) for 4 consecutive days and serum samples analysed 60 days later. Results are representative of 2 independent experiments. All data are presented as mean values ± s.e.m., statistical significance calculated by 2-way ANOVA with Šidák's multiple comparison test (**b**, **e**, **f**, **g**) or two-tailed Mann-Whitney test (**a**) or ordinary 1-way ANOVA (CFUs) or 2-way ANOVA (serum) with Tukey's multiple comparison test (**c**). The schematic in **c** was created using graphical templates from Servier Medical Art under a Creative Commons licence CC BY 4.0 (https://creativecommons.org/licenses/by/4.0/).

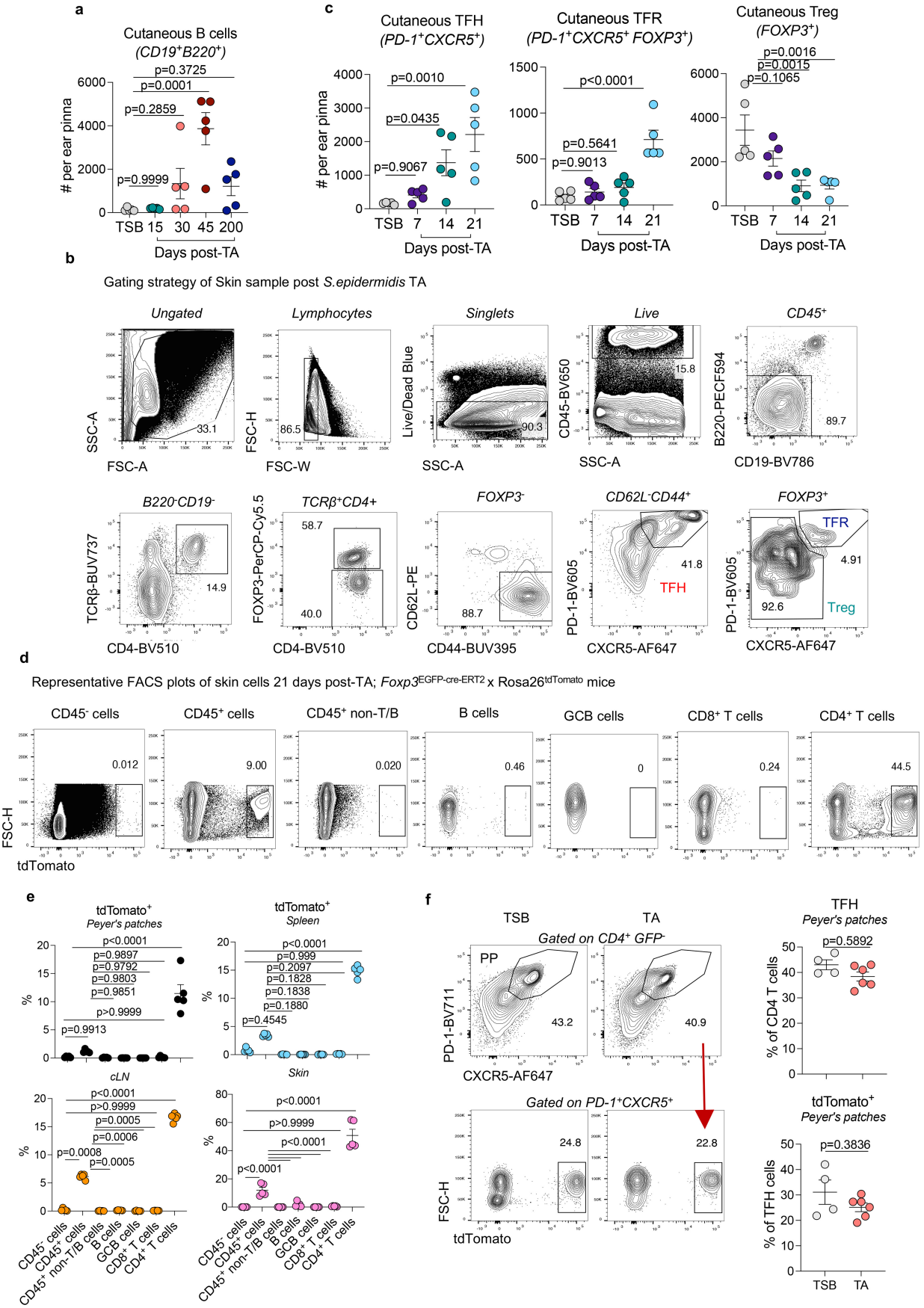

Extended Data Fig. 2 | See next page for caption.

Extended Data Fig. 2 | Topical association promotes cutaneous B cell and CD4$^+$ T cell accumulation. a, Skin B cell (B220$^+$CD19$^+$) absolute numbers per ear pinna as analysed by flow cytometry in unassociated (TSB) or associated (TA) WT mice; n = 5. **b**, Gating strategy of skin CD4$^+$ T cells as shown; T_{regs} (FOXP3$^+$CXCR5$^-$), T_{FR} (FOXP3$^+$CXCR5$^+$PD-1$^+$) and T_{FH} cells (FOXP3$^-$PD-1$^+$CXCR5$^+$). **c**, Absolute numbers of T_{FH}, T_{FR} and T_{reg} cells in the skin of unassociated (TSB), and associated (Day 7, 14, 21) WT mice per ear pinna as shown by flow cytometry; n = 5. **d-f**, *Foxp3*$^{EGFP\text{-}cre\text{-}ERT2}$ x Rosa26^{tdTomato} mice treated with oral tamoxifen 5 days before the association with *S.epidermidis* and cell phenotyping performed 21 days post-TA. **d**,**e**, tdTomato expression among CD45 negative cells and various populations of CD45$^+$ cells in skin, cLN, Peyer's patches (PP) and spleen; n = 5. **d** – representative FACS plots of skin subpopulations, **e** – summary graphs showing percentage of tdTomato expression in skin, cLN, PP and spleen. **f**, Representative FACS plots of T_{FH} cells in PP and graphs depicting overall percentage of T_{FH} cells among CD4$^+$ T cell population and tdTomato expressing cells among T_{FH} cells; n = 4 (TSB), 6 (TA). All data are presented as mean values ± s.e.m., statistical significance calculated by 1-way ANOVA with Dunnet's multiple comparison test (**a**, **c**), or 2-way ANOVA with Tukey's multiple comparison test (**e**) or 1-way ANOVA with Tukey's multiple comparison test (**f**).

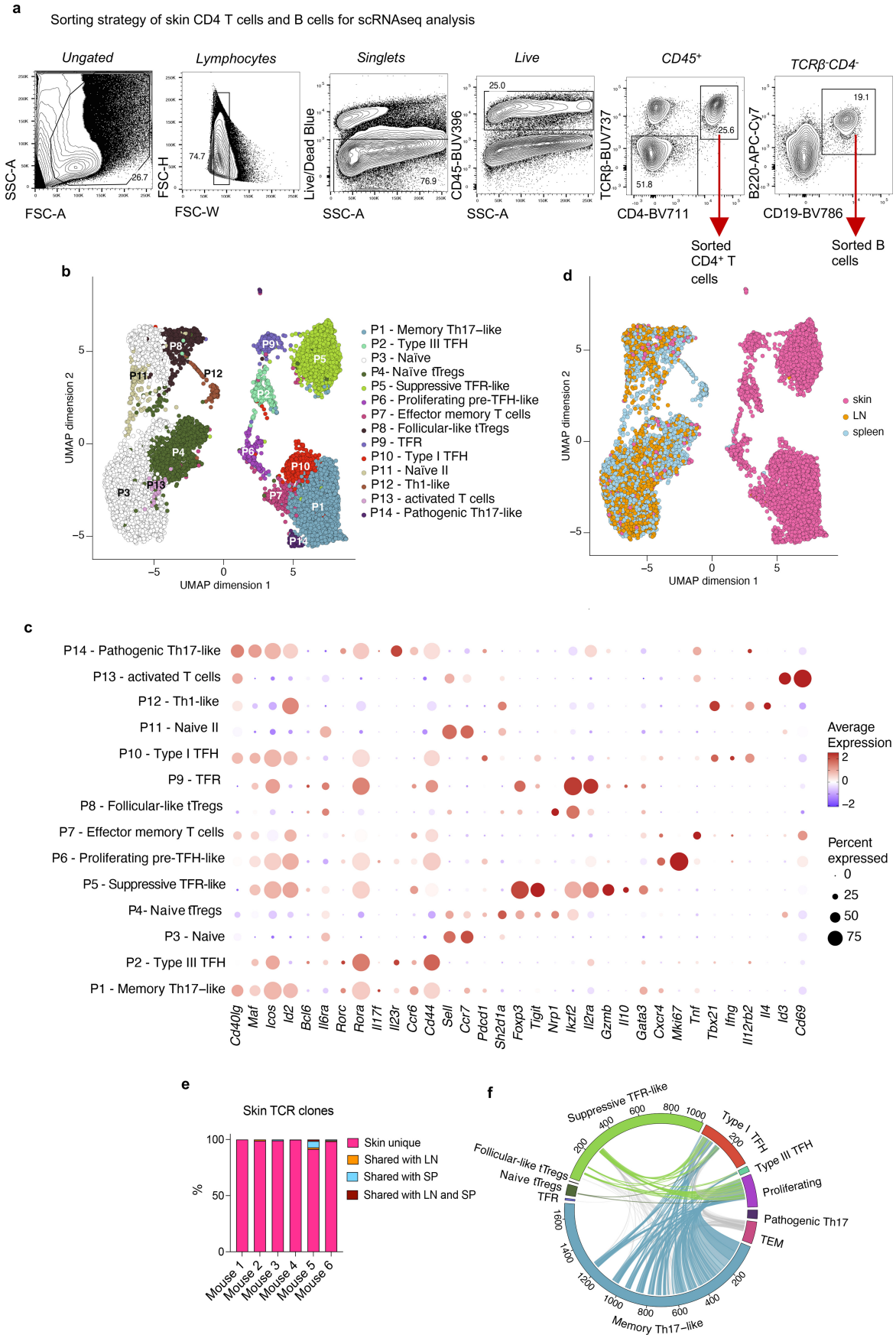

Extended Data Fig. 3 | See next page for caption.

Extended Data Fig. 3 | Transcriptional profiling of cutaneous CD4$^+$ T cells. **a-f**, C57BL/6 WT mice topically associated with *S.epidermidis* and 21 days later CD4$^+$ T cells from skin, skin draining LN and spleen were sorted for scRNAseq analysis. **a**, Sorting strategy of cutaneous B cells and CD4$^+$ T cells. **b**, UMAP representation of pooled skin, LN and spleen CD4$^+$ T cells from 6 mice. A total of 14 different clusters were identified. **c**, Dot plot showing average expression and proportion of expression of signature genes in all clusters used for cell type annotation. **d**, UMAP representation of population division by organ – skin (pink), LN (orange), spleen (blue). **e**, Bar graph depicting skin TCR clone overlap with SP and/or LN. **f**, Circular plot showing TCR clonotype sharing between populations in the skin. Results are representative of 2 independent experiments.

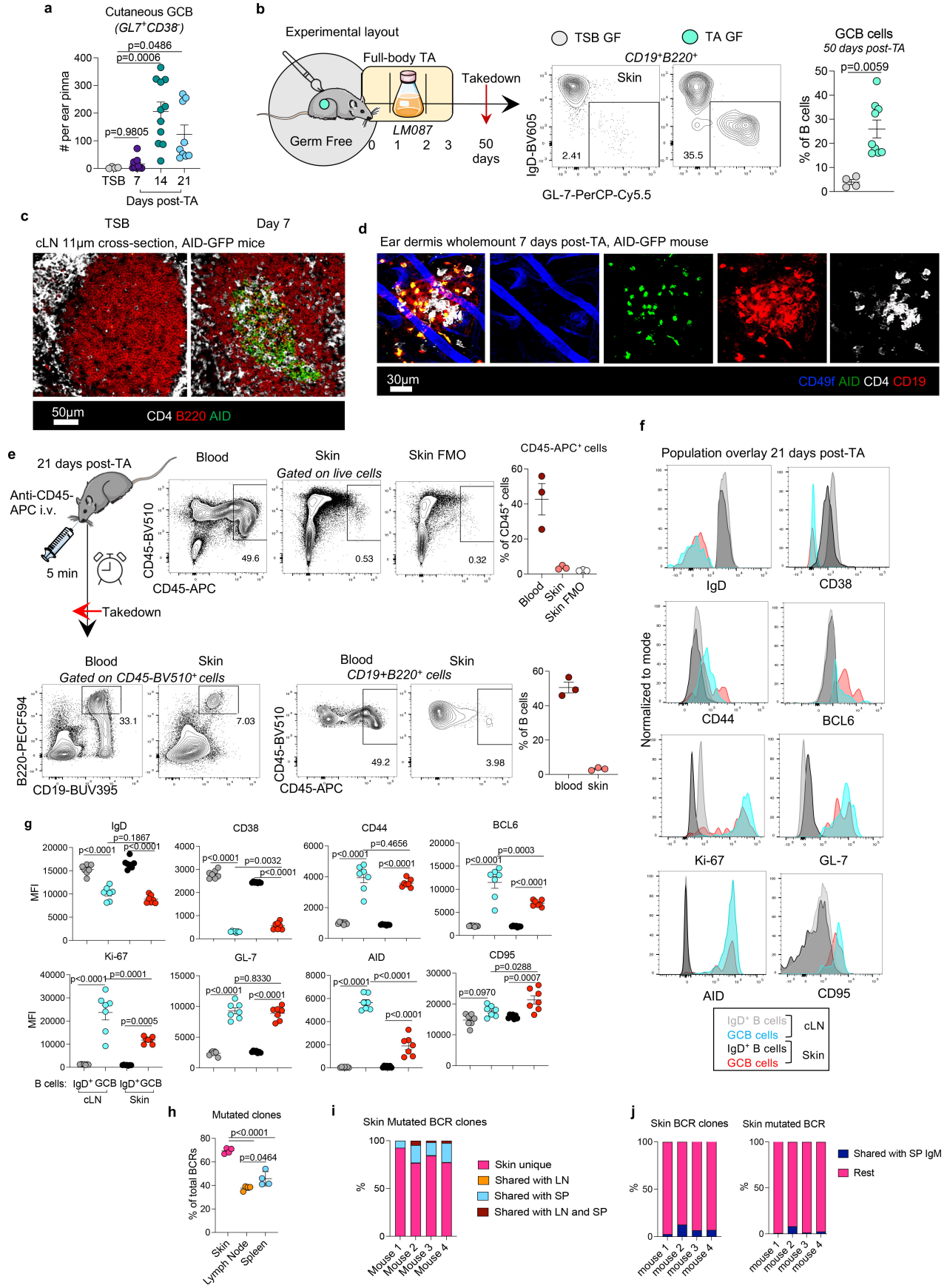

Extended Data Fig. 4 | See next page for caption.

Extended Data Fig. 4 | Topical association triggers germinal centre B cell accumulation in the skin. a, Absolute number of germinal centre B cells ($GL\text{-}7^+CD38^-$) in the skin of unassociated (TSB), and associated (Day 7, 14, 21) WT mice per ear pinna as shown by flow cytometry; n = 4 (TSB), 11 (Day 7, 14), 9 (Day 21). **b**, C57BL/6 germ-free mice topically associated with *S.epidermidis* LM087 and 50 days later skin GCB cells (IgD negative $GL\text{-}7^+$) analyzed by flow cytometry; n = 4 (TSB), 9 (TA). **c**, AID expression in frozen cLN cross-section 7 days post-TA compared to unassociated (TSB) AID-eGFP reporter mouse; B220 (red), CD4 (white), AID (green), 11 µm thickness; scale: 50 µm. **d**, AID expression in ear dermis wholemount of AID-eGFP reporter mouse 7 days post-TA; CD49f (blue), AID (green), CD19 (red), CD4 (white), scale: 30 µm. **e**, C57BL/6 WT mice topically associated with *S.epidermidis* 21 days prior the administration of 2 µg of anti-CD45-APC antibody (eBioscience, clone 30-F11) intravenously and mice euthanized 5 min later. APC labelling of blood and skin lymphocytes assessed via flow cytometry; n = 3. **f-g**, MFI of CD95, GL-7, Ki-67, AID, BCL6, CD44, CD38 and IgD expression within GCB and naive skin and cLN B cells of WT C57BL/6 mice 21 days after *S.epidermidis* TA; n = 7. **h-j**, BCR-seq of total RNA extracted from skin, cLN and spleen of WT mice 30 days post-TA. **h**, Graph depicting the percentage of mutated BCR clones among all BCR clones per organ. **i**, Bar graph showing skin mutated BCR overlap with BCRs in spleen and/or LN within individual mice. **j**, Bar graph showing skin total and mutated BCR overlap with BCRs from splenic IgM B cells within individual mice; n = 4. Results are representative of 2-5 independent experiments. All data are presented as mean values ± s.e.m., statistical significance calculated by 1-way ANOVA with Dunnet's multiple comparison test (**a**, **b**) or ordinary 1-way ANOVA with Tukey's multiple comparison test (**g**, **h**). The schematics in **b**,**e** were created using graphical templates from Servier Medical Art under a Creative Commons licence CC BY 4.0 (https://creativecommons.org/licenses/by/4.0/).

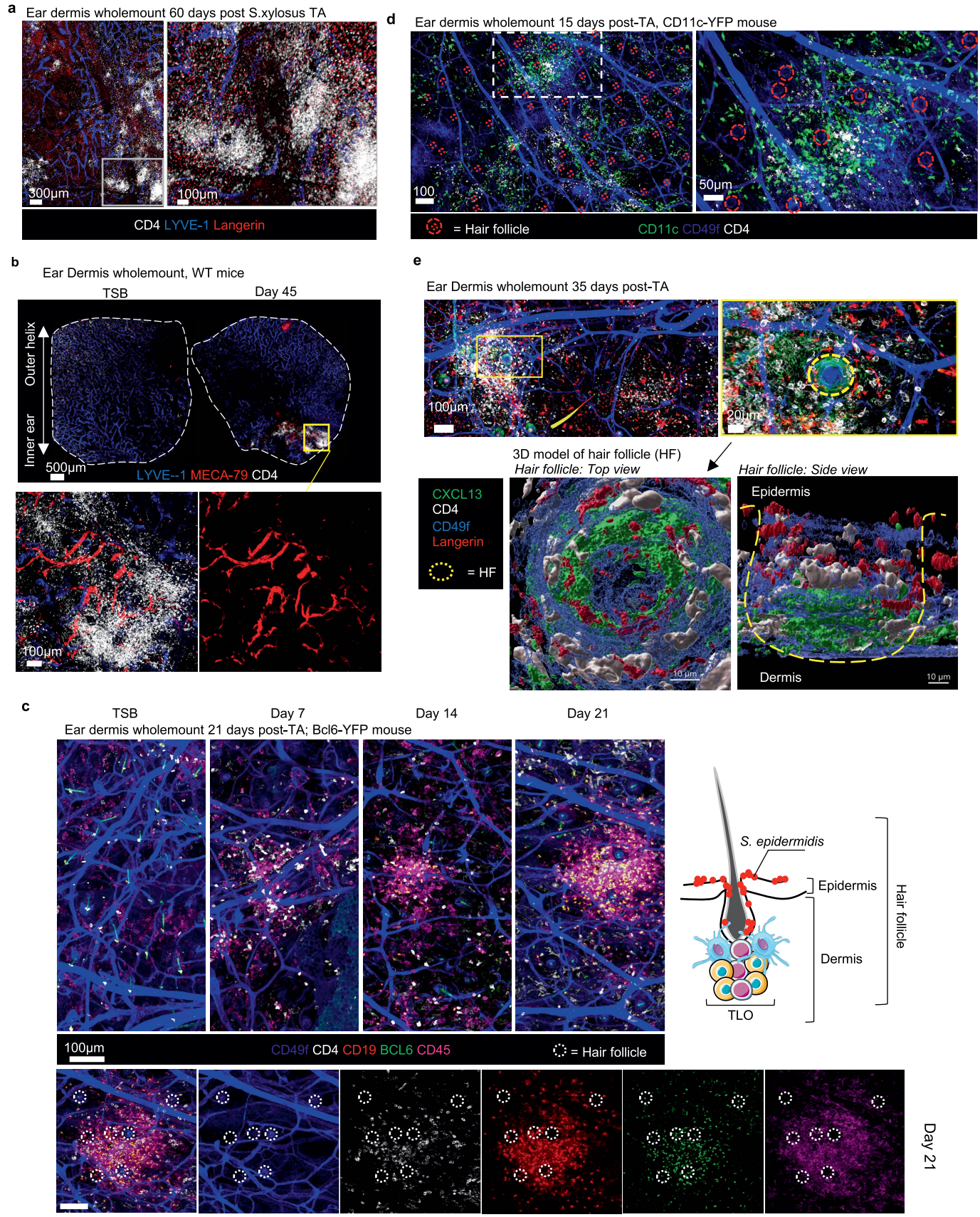

Extended Data Fig. 5 | See next page for caption.

Extended Data Fig. 5 | Dermal TLOs are associated with HEVs and Langerhans cells. a, C57BL/6 mice associated with *Staphylococcus xylosus* for 4 times and 50 days later ear dermis wholemounts imaged: CD4 (white), LYVE-1 (blue) and Langerin (red); results reproduced in 10 mice. **b**, Confocal image of the entire ear of ear dermis wholemount of control (TSB) and *S.epidermidis* LM087 associated (45 days) WT mice (CD4 (white), MECA-79 (red), and LYVE-1 (blue)) scale:500 µm (whole ear), 100 µm (magnification); observation confirmed in over 20 mice. **c**, Cutaneous lymphocyte (CD4 (white), CD19 (red), BCL6 (green), CD45 (magenta)) reorganization into tertiary lymphoid organs (TLO) in ear dermis (CD49f (blue)) wholemount 7, 14, 21 days post-TA with LM087 in comparison to unassociated (TSB) control of Bcl6-YFP reporter mouse as shown by confocal imaging, scale:100 µm; punctuated circles within day 21 TLO mark hair follicles; schematic representation of hair follicle cross-section (upper right); observation confirmed in over 20 mice. **d**, Ear dermis wholemount of CD11c-YFP reporter mouse 15 days post-TA (CD11c (green), CD4 (white), CD49f (blue)), scale:100 µm, magnification: 50 µm; red circles indicate hair follicles; observation confirmed in 10 mice. **e**, Confocal image and its 3D reconstruction of ear dermis wholemount showing CXCL13 expression (green), CD4 (grey), CD49f (blue) and Langerin (red) in WT mouse 35 days post-TA - punctuated circle marks the hair follicles; scale: 100 µm (confocal; magnified: 20 µm), 10 µm (reconstruction). Observation confirmed in 10 mice. The schematic in **c** was created using graphical templates from Servier Medical Art under a Creative Commons licence CC BY 4.0 (https://creativecommons.org/licenses/by/4.0/).

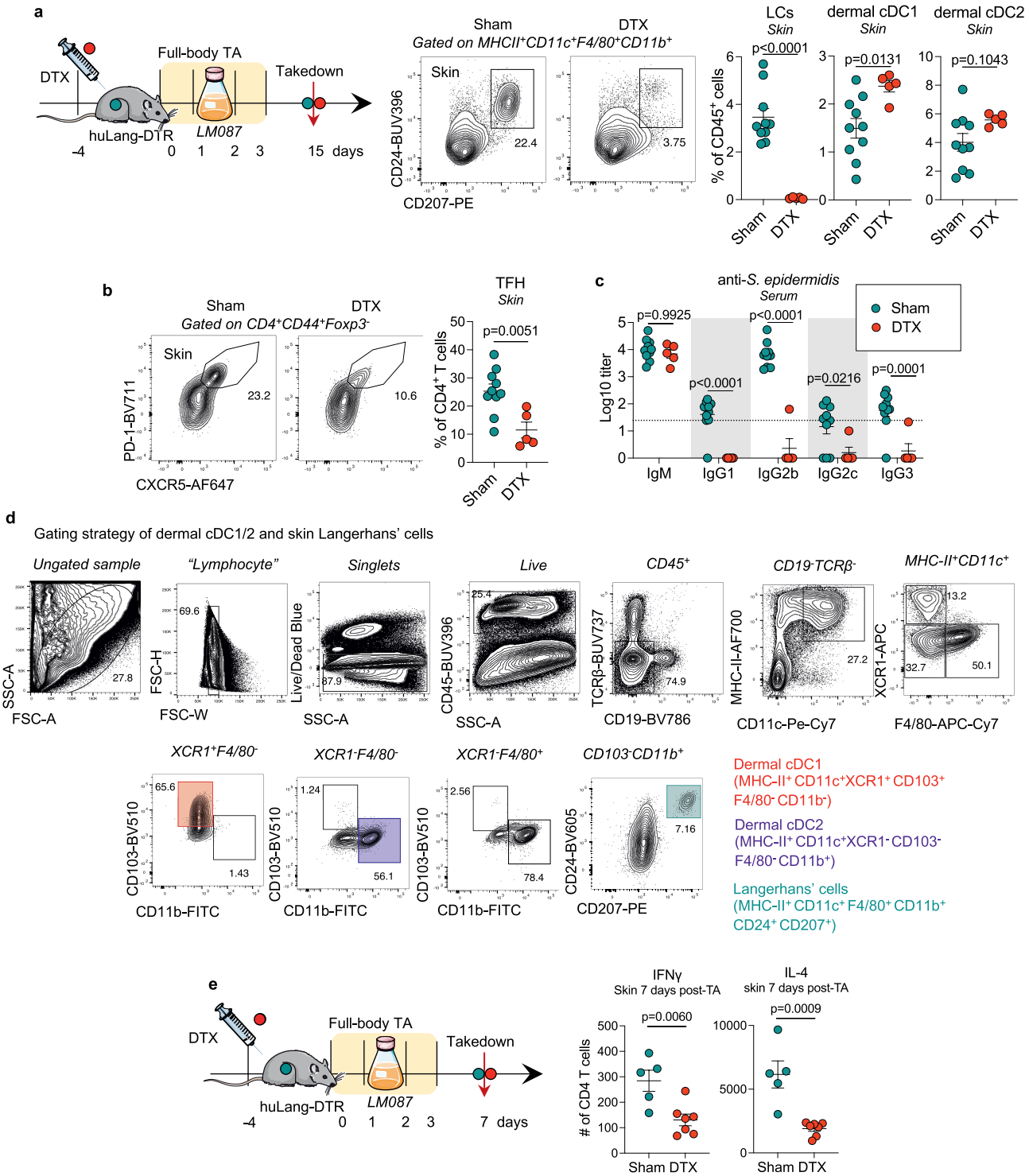

Extended Data Fig. 6 | Humoral immunity in response to skin colonization forms in Langerhans cell dependent-manner. a-c, huLang-DTR mice treated with or without (sham; n = 10) Diphtheria toxin (DTX; n = 5) intraperitoneally 4 days before the topical association with *S. epidermidis* and samples analysed 14 days later as shown in the scheme (**a**). Representative FACS plots of skin Langerhans cells ($CD207^+CD24^+$), and frequencies of Langerhans cells, dermal cDC1 and cDC2 cells within skin $CD45^+$ population. **b**, Representative FACS plots and T_{FH} frequencies in skin analysed by flow cytometry. **c**, IgM, IgG1, IgG2b, IgG2c, and IgG3 serum reactivity to *S. epidermidis* was measured as log10 titres via ELISA assay. **d**, Example of the gating strategy of dermal cDC1 ($XCR1^+CD103^+CD11b^-F4/80^-$), dermal cDC2 ($XCR1^-CD103$-$CD11b^+F4/80^-$), and Langerhans cells ($XCR1^-CD103^-CD11b^+F4/80^+CD24^+CD207^+$) as shown. **e**, huLang-DTR mice were depleted (or not; sham) of LCs 4 days prior to the topical association with *S.epidermidis*; absolute numbers of cytokine-producing skin $CD4^+$ T cells were assessed by flow cytometry on day 7; n = 5 (Sham), 7 (DTX). Results are representative of 3 independent experiments showing similar results. All data are presented as mean values ± s.e.m., statistical significance calculated by two-tailed unpaired t test (**a**, **b**, **e**), or 2-way ANOVA with Šidák's multiple comparison test (**c**). The schematics in **a**,**e** were created using graphical templates from Servier Medical Art under a Creative Commons licence CC BY 4.0 (https://creativecommons.org/licenses/by/4.0/).

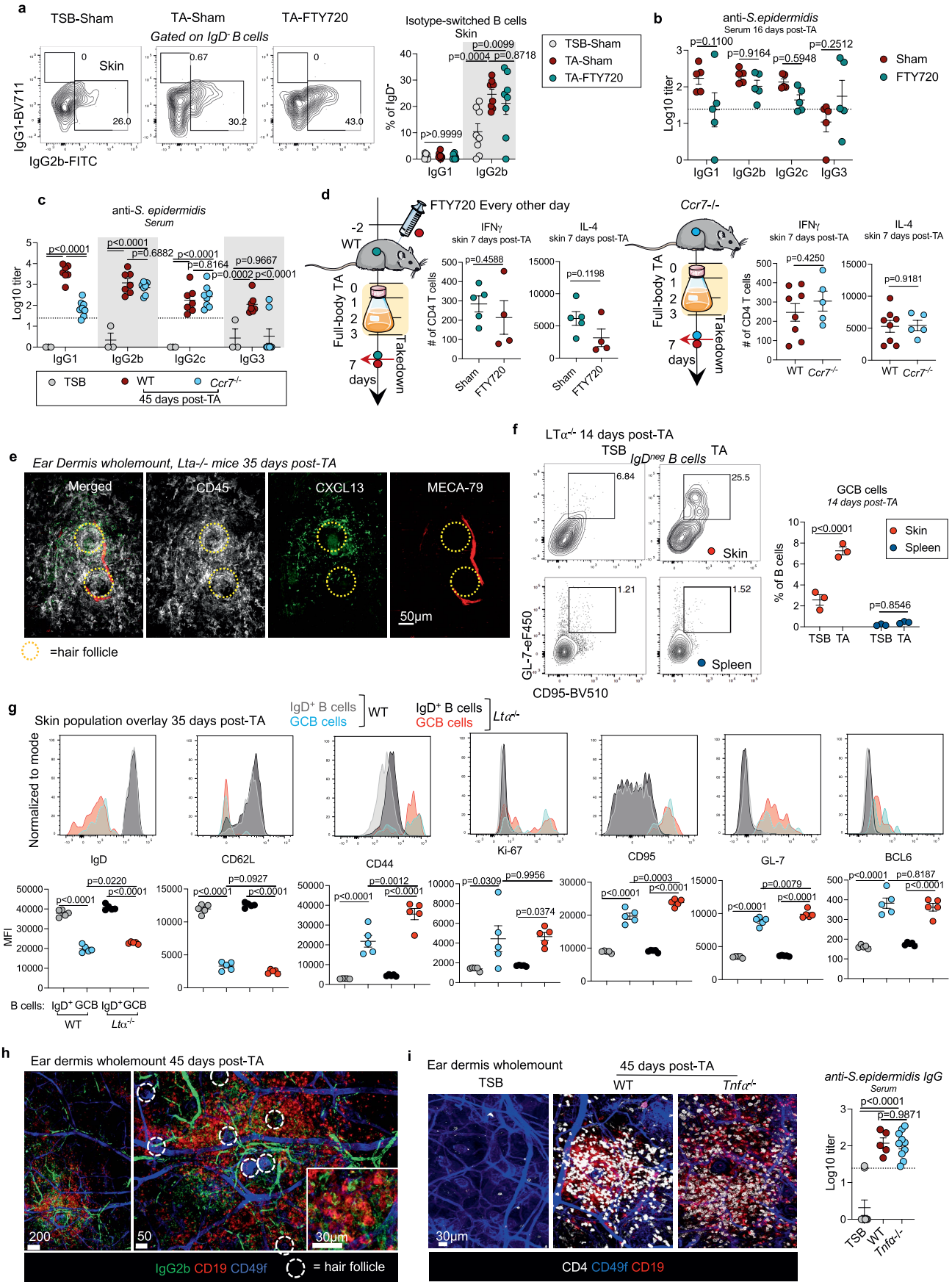

Extended Data Fig. 7 | See next page for caption.

Extended Data Fig. 7 | Humoral immunity to *S. epidermidis* occurs independently of draining LN. a,**b**, WT C57BL/6 mice treated with or without (sham) FTY720 intraperitoneally 2 days before the topical association with *S. epidermidis* and continuously every other day throughout the experiment, samples analysed 16 (**b**) or 45 (**a**) days post-TA. **a**, Representative FACS plots and frequencies of skin class-switched IgG1$^+$ and IgG2b$^+$ cells analysed by flow cytometry; n = 8. **b**, IgG1, IgG2b, IgG2c, and IgG3 serum reactivity to *S. epidermidis* measured as log10 titres via ELISA assay; n = 5. **c**, WT and *Ccr7*$^{-/-}$ mice compared for serum reactivity to *S. epidermidis* 45 days post-TA; antibodies measured as log10 titres via ELISA assay; n = 3 (TSB), 7 (WT), 8 (*Ccr7*$^{-/-}$). **d**, C57BL/6 WT mice treated with FTY720 2 days prior to the association and continuously every other day through the experiment (n = 5 (Sham), 4 (FTY720)); *Ccr7*$^{-/-}$ mice topically associated n = 8 (WT), 5 (*Ccr7*$^{-/-}$). Absolute numbers of cytokine-producing skin CD4$^+$ T cells assessed by flow cytometry 7 days later. **e**-**g**, *Lta*$^{-/-}$ mice topically associated with *S.epidermidis* LM087 or TSB. **e**, Ear dermis wholemount imaged 35 days post-TA; CXCL13 (green), CD4 (white), MECA-79 (red), punctuated circles mark hair follicles; scale: 50µm; observation confirmed in 5 mice. **f**, Skin and splenic B cells analysed via flow cytometry 14 days post-TA. Representative FACS plots and corresponding GCB cell frequency shown; n = 3. **g**, Expression level of CD95, GL-7, Ki-67, CD62L, BCL6, CD44 and IgD compared between skin GCB and naïve B cells in WT and *Lta*$^{-/-}$ mice 35 days post-TA; n = 5. **h**, Confocal image of TLO within ear dermis wholemount 45 days post-TA; CD19(red), IgG2b (green) CD49f (blue), zoomed-in scale:30 µm; observation confirmed in over 20 mice. **i**, Confocal image of TLO within ear dermis wholemount of WT and *Tnfα*$^{-/-}$ mice 45 days post-TA; CD4 (white), CD19(red), CD49f (blue), scale:30 µm; serum response to skin colonization in these mice calculated as log10 titre; n = 9 (TSB), 5 (WT), 10 (*Tnfα*$^{-/-}$). Results are representative of 3 independent experiments. All data are presented as mean values ± s.e.m., statistical significance calculated by 2-way ANOVA with Šidák's (**a**, **b**, **f**) or Tukey's (c, g) multiple comparison test or ordinary 1-way ANOVA with Tukey's multiple comparison test (**i**) or by two-tailed unpaired t test (**d**). The schematics in **d** were created using graphical templates from Servier Medical Art under a Creative Commons licence CC BY 4.0 (https://creativecommons.org/licenses/by/4.0/).

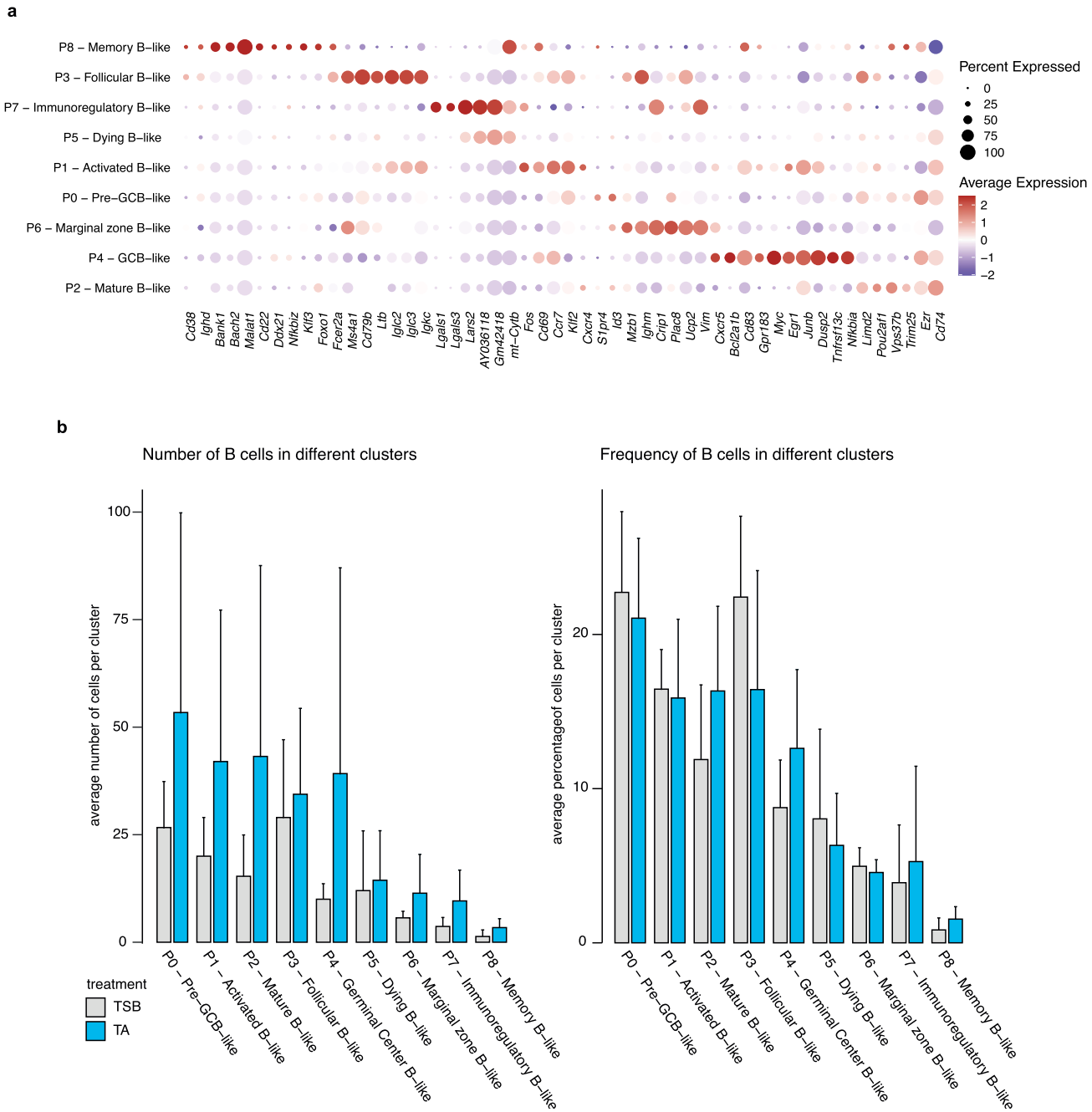

Extended Data Fig. 8 | Transcriptional profiling of cutaneous B cells in *Lta*$^{-/-}$ mice. a, *Lta*$^{-/-}$ mice associated with *S.epidermidis* LM087 (n = 5) or TSB (n = 3) and 14 days later cutaneous B cells sorted (as shown in Extended Data Fig. 3a); obtained cells pooled for single cell RNA-seq analysis and a total of 9 different clusters identified. Dot plot showing average expression and proportion of expression of signature genes in all clusters used to annotate cell types. **b**, Expansion profile of individual clusters between TSB and TA treatment; data are presented as mean values +/− SD.

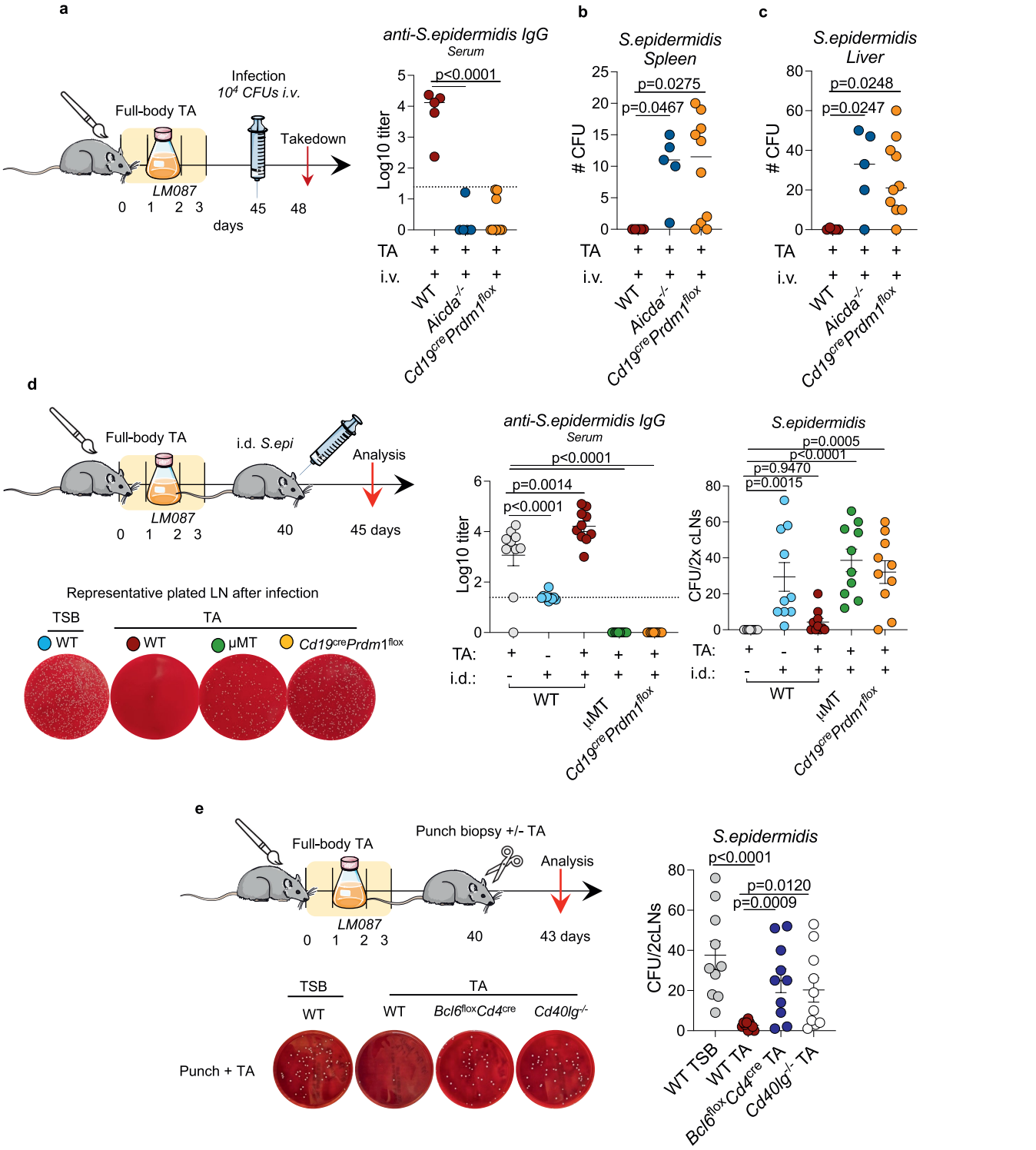

Extended Data Fig. 9 | Colonization-induced antibodies provide systemic protection. a-c, WT C57BL/6, *Aicda*$^{-/-}$, and *Cd19*^{cre}*Prdm1*^{flox} mice topically associated and 45 days later infected intravenously with 10^4 CFU *S. epidermidis*, samples analysed 3 days later as shown in the scheme: n=5 (WT and *Aicda*$^{-/-}$), 10 (*Cd19*^{cre}*Prdm1*^{flox}) (**a**). IgG serum reactivity to *S. epidermidis* was measured as log10 titres via ELISA assay (**a**); spleen (**b**) and liver (**c**) colonizing *S. epidermidis* CFUs enumerated per organ. **d**, WT C57BL/6, µMT and *Cd19*^{cre}Prdm1^{cre} mice topically associated and 40 days later infected intradermally with 10^6 CFU *S. epidermidis*, samples analysed 5 days later as shown in the scheme; n = 10; positive control: TSB WT infected, negative control: TA WT uninfected. IgG serum reactivity to *S. epidermidis* was measured as log10 titres via ELISA assay and *S.epidermidis* CFUs in skin draining LN enumerated. **e**, WT C57BL/6, *Bcl6*^{flox}*Cd4*^{cre} and *Cd40lg*$^{-/-}$ mice topically associated and 40 days later punch biopsies of ear skin performed; mice reassociated with *S.epidermidis* as shown in the scheme. Bacterial translocation to skin draining LN quantified 3 days later; n = 10. Results are representative of 2 independent experiments. All data are presented as mean values ± s.e.m., statistical significance calculated by ordinary 1-way ANOVA with Dunnett's multiple comparison test (**a-e**). The schematics in **a**,**d**,**e** were created using graphical templates from Servier Medical Art under a Creative Commons licence CC BY 4.0 (https://creativecommons.org/licenses/by/4.0/).

Corresponding author(s): Yasmine Belkaid, Inta Gribonika

Last updated by author(s): Oct 22, 2024

Reporting Summary

Nature Portfolio wishes to improve the reproducibility of the work that we publish. This form provides structure for consistency and transparency in reporting. For further information on Nature Portfolio policies, see our Editorial Policies and the Editorial Policy Checklist.

Statistics

For all statistical analyses, confirm that the following items are present in the figure legend, table legend, main text, or Methods section.

n/a	Confirmed	
☐	☒	The exact sample size (*n*) for each experimental group/condition, given as a discrete number and unit of measurement
☐	☒	A statement on whether measurements were taken from distinct samples or whether the same sample was measured repeatedly
☐	☒	The statistical test(s) used AND whether they are one- or two-sided *Only common tests should be described solely by name; describe more complex techniques in the Methods section.*
☒	☐	A description of all covariates tested
☒	☐	A description of any assumptions or corrections, such as tests of normality and adjustment for multiple comparisons
☐	☒	A full description of the statistical parameters including central tendency (e.g. means) or other basic estimates (e.g. regression coefficient) AND variation (e.g. standard deviation) or associated estimates of uncertainty (e.g. confidence intervals)
☐	☒	For null hypothesis testing, the test statistic (e.g. *F*, *t*, *r*) with confidence intervals, effect sizes, degrees of freedom and *P* value noted *Give P values as exact values whenever suitable.*
☒	☐	For Bayesian analysis, information on the choice of priors and Markov chain Monte Carlo settings
☒	☐	For hierarchical and complex designs, identification of the appropriate level for tests and full reporting of outcomes
☒	☐	Estimates of effect sizes (e.g. Cohen's *d*, Pearson's *r*), indicating how they were calculated

Our web collection on statistics for biologists contains articles on many of the points above.

Software and code

Policy information about availability of computer code

Data collection

For flow cytometry data acquisition LSRFortessa (BD Biosciences) cell analyzer with BD FACSDiva v9.0 software was used. For cell sorting FACSAria Fusion (BD Biosciences) cell sorter was used.
Elisa plates were acquired by BioTek Synergy H1 microplate reader supplied with Gen5 3.14 software.
Elispot plates were read and counted using an ImmunoSpot analyzer (CTL) with CTL Switchboard 2.6.1
Confocal Microscopy was perfomed on Leica TCS SP8 confocal microscope with LAS X software platform.
scRNAseq data generated using 10x Genomics Chromium platform and sequenced using Illumina NextSeq 2000 and 1000 platforms.

Data analysis	Illumina files were converted to FASTQ files using bcl-output command v3.10.5 and data were filtered and mapped to mm10 reference genome (https://cf.10xgenomics.com/supp/cell-exp/refdata-gex-mm10-2020-A.tar.gz) by using Cell Ranger v7.1.0 (10X Genomics). For scRNA-seq analysis following softwares were used: bcl-output command v3.10., Seurat v. 5.0.2 (for scRNA-seq of T cells), scRepertoire v.2.0.0, circlize (v.0.4.15), Seurat version 3.1/4.1.0 (for scRNA-seq of B cells), R package scuttle (v1.4.0) BCR sequencing raw data was analyzed using the iRmap v3.0 software (iRepertoire). Merged reads were mapped to germline V, D, J, and C reference sequences using the IMGT reference library (https://www.imgt.org). For FACS analysis FlowJo v. 10.8.2 was used For microscopy data Imaris Bitplane software v. 10.0 was used For data visualization GraphPad Prim 9, MS Powerpoint v.16.79.1 and Adobe Illustrator v. 28.0 was used. The codes used to analyze sequencing data are made available and can be accessed via link in Code Availability Statement.

For manuscripts utilizing custom algorithms or software that are central to the research but not yet described in published literature, software must be made available to editors and reviewers. We strongly encourage code deposition in a community repository (e.g. GitHub). See the Nature Portfolio guidelines for submitting code & software for further information.

Data

Policy information about availability of data

All manuscripts must include a data availability statement. This statement should provide the following information, where applicable:

- Accession codes, unique identifiers, or web links for publicly available datasets
- A description of any restrictions on data availability
- For clinical datasets or third party data, please ensure that the statement adheres to our policy

Single cell RNA-seq data and Seurat objects for B cells are available under GEO accession number GSE250572, single cell RNA-seq data and Seurat objects for T cells are available under GEO accession number GSE272390 and bulk BCR-sequencing data and processed chain data is available under GEO accession number GSE279095. All BCR clonotype sequences are summarized as Supplementary Table 2 and all BCR clonotype sequences with SHM are summarized as Supplementary Table 3, deposited at Zenodo repository and can be accessed at https://zenodo.org/records/13987214.

Research involving human participants, their data, or biological material

Policy information about studies with human participants or human data. See also policy information about sex, gender (identity/presentation), and sexual orientation and race, ethnicity and racism.

Reporting on sex and gender	Human samples, participants or data were not used for this study.
Reporting on race, ethnicity, or other socially relevant groupings	Not applicable
Population characteristics	Not applicable
Recruitment	Not applicable
Ethics oversight	Not applicable

Note that full information on the approval of the study protocol must also be provided in the manuscript.

Field-specific reporting

Please select the one below that is the best fit for your research. If you are not sure, read the appropriate sections before making your selection.

☒ Life sciences ☐ Behavioural & social sciences ☐ Ecological, evolutionary & environmental sciences

For a reference copy of the document with all sections, see nature.com/documents/nr-reporting-summary-flat.pdf

Life sciences study design

All studies must disclose on these points even when the disclosure is negative.

Sample size	When possible, preliminary experiments were performed to determine requirements for sample size, considering resources available and ethical, reductionist animal use. All experiments were performed with at least 3 mice/group (negative control, TSB throughout the manuscript) or as many as 14 mice (experimental TA treated group). On average, 5 mice were used/experimental group. For each experiment number of animals used is noted in the figure legend.
Data exclusions	Data were excluded from the sample only if an inadequate staining or low cell yield due to technical problems was observed.

Replication	Each experiment was repeated 2-5 times as stated in the figure legend.
Randomization	Animals were assigned randomly to experimental groups.
Blinding	Some, but not all experiments were performed blindly with data acquisition done before the genotyping of the specific mouse strain. Then acquired data was matched with genotyping results and plotted. This project was initiated during the global pandemic when many labs experienced shortages in laboratory plastic wear supplies. Hence, in situations like these, animals were euthanized and tissues harvested based on known groups to limit plastic usage for each experiment. Post-pandemic, when situation normalized, mice although treated within known groups were blinded at the sacrifice - cage cards removed and tissues harvested without actual knowledge whether specific cage was TSB treated or associated with bacteria. Then based on bacterial CFUs plated on Columbia Agar plates and serum ELISA readouts it was determined whether acquired FACS data and microscopy samples are from TA or TSB mice and then matched with the animal facility records. This however could be done only at the sacrifice and not during the treatment phase to avoid the cross- contamination of treated mice with those of negative control group during the experiement. Upon treatment, bacteria establish residency with its host and can be passively acquired by non-treated mouse (see figure 1e). For this reason we could not blind the experiment during initiation phase as each group had to be kept and handled separately while caged in the animal facility (animal technicians were asked to change gloves between each cage and animals were handled with forceps to avoid contact with animal's skin). All mice prior to the experiment and irrespective of the vendor were cohoused for 2 weeks to normalize the microbiota.

Reporting for specific materials, systems and methods

We require information from authors about some types of materials, experimental systems and methods used in many studies. Here, indicate whether each material, system or method listed is relevant to your study. If you are not sure if a list item applies to your research, read the appropriate section before selecting a response.

Materials & experimental systems

n/a	Involved in the study
☐	☒ Antibodies
☒	☐ Eukaryotic cell lines
☒	☐ Palaeontology and archaeology
☐	☒ Animals and other organisms
☒	☐ Clinical data
☒	☐ Dual use research of concern
☒	☐ Plants

Methods

n/a	Involved in the study
☒	☐ ChIP-seq
☐	☒ Flow cytometry
☒	☐ MRI-based neuroimaging

Antibodies

Antibodies used	For flow cytometry, cells were stained with the following antibodies: hamster anti-mouse TCRβ-BUV737 (H57-597, BD Horizon, cat# 612821, 1/400), rat anti-mouse IFNg-BV421 (XMG1.2, BD Horizon, cat# 563376, 1/100), rat anti-mouse IL-4-PE (11B11, Biolegend, cat# 504103, 1/100), rat anti-mouse CD4-BV711 (GK1.5, BD Horizon, cat# 563050, 1/400), rat anti-mouse CD4-BV510 (RM4-5, BD Horizon, cat# 563106, 1/500), rat anti-mouse CD4-BV650 (RM4-5, BD Horizon, cat# 563747, 1/400), rat anti-mouse CD62L-BV605 (MEL-14, BD Horizon, cat# 563252, 1/600), rat anti-mouse CD62L-PE (MEL-14, BioLegend, cat# 104407, 1/500), rat anti-mouse CD45-BUV396 (30-F11, BD Horizon, cat# 564279, 1/300), rat anti-mouse CD45-BV650 (30-F11, BD Horizon, cat# 563410, 1/300), rat anti-mouse CD45-APC (30-F11, eBioscience, cat# 17-0451-82, 1/400), rat anti-mouse CD45-BV510 (30-F11, BD Horizon, cat# 563891, 1/400), rat anti-mouse CD24-BUV396 (M1/69, BD OptiBuild, cat# 744471, 1/200), rat anti-mouse CD24-BV605 (M1/69, BD Horizon, cat# 563060, 1/200), mouse anti-BCL6-AF488 (K112-91, BD Pharmingen, cat# 561524, 1/100), rat anti-mouse CXCR5-AF647 (L138D7, BioLegend, cat# 145531, 1/100), hamster anti-mouse PD-1-BV711 (J43, BD OptiBuild, cat# 744547, 1/200), rat anti-mouse PD-1-BV605 (29F.1A12, BioLegend, cat# 135219, 1/200), rat anti-mouse/human ki-67-Pe-cy7 (SolA15, eBioscience (ThermoFisherScientific, cat# 25-5698-82, 1/300), rat anti-mouse IgD-PerCP-Cy5.5 (11-26c.2a, BioLegend, cat# 405709, 1/800), rat anti-mouse IgD-BV605 (11-26c.2a, BioLegend, cat# 405727, 1/600), rat anti-mouse IgG1-BV711 (A85-1, BD Horizon, cat# 565786, 1/200), rat anti-mouse IgG2b-FITC (R12-3, BD Pharmingen, cat# 553395, 1/200), rat anti-mouse B220-PECF594 (RA3-6B2, BD Horizon, cat# 562313, 1/400), rat anti-mouse B220-APC-Cy7 (RA3-6B2, BD Horizon, cat# 552094, 1/400), rat anti-mouse CD19-BUV396 (1D3, BD Horizon, cat# 563557, 1/300), rat anti-mouse CD19-BV785 (6D5, BioLegend, cat# 115543, 1/300), rat anti-mouse/human GL-7-eF450 (GL7, eBioscience (ThermoFisherScientific, cat# 48-5902-82, 1/200), rat anti-mouse/human GL-7-PerCP-Cy5.5 (GL7, Biolegend, cat# 144609, 1/200), rat anti-mouse CD38-APC (90, BioLegend, cat# 102711, 1/300), hamster anti-mouse CD95-BV510 (Jo2, BD Horizon, cat# 563646, 1/300), rat anti-mouse/hamster/human Foxp3-AF700 (FJK-16s, eBioscience (ThermoFisherScientific,) cat# 56-5773-82, 1/100), rat anti-mouse Foxp3-PerCP-Cy5.5 (R16-715, BD Pharmingen, cat# 563902, 1/100), rat anti-mouse MHCII-AF700 (M5/114.15.2, eBioscience (ThermoFisherScientific), cat# 56-5321-82, 1/200), rat anti-mouse CD11b-FITC (M1/70, eBioscience (ThermoFisherScientific), cat# 11-0112-82, 1/200), hamster anti-mouse CD11c-PeCy7 (N418, BioLegend, cat# 117317, 1/200), rat anti-mouse Langerin (CD207)-PE (929F3.01, Dendritics corp, cat# DDX0362P-100, 1/200), rat anti-mouse CD44-BUV395 (IM7, BD OptiBuild, cat# 740215, 1/400), rat anti-mouse CD44-Pe-Cy7 (IM7, BD Pharmingen, cat# 560569, 1/400), rat anti-mouse CD103-BV510 (M290, BD Horizon, cat# 563087, 1/200), mouse anti-mouse/rat XCR1-APC (ZET, BioLegend, cat# 148205, 1/200), rat anti-mouse F4/80-APC-Cy7 (BM8, BioLegend, cat# 123117, 1/200), and rat anti-mouse CD25-Per-CP-Cy5.5 (PC61.5, eBioscience (ThermoFisherScientific), cat# 45-0251-82, 1/200). For ELISA and Elispot assays antibodies conjugated to alkaline phosphatase (AP) from SouthernBiotech were used: goat anti-mouse IgG1-AP (cat# 1071-04, 1/1000), goat anti-mouse IgA-AP (cat# 1040-04, 1/1000), goat anti-mouse IgM-AP (cat# 1021-04, 1/1000), goat anti-mouse IgG-AP (cat# 1036-04, 1/1000), goat anti-mouse IgG2b-AP (cat# 1091-04, 1/1000), goat anti-mouse IgG2c-AP (cat#

1079-04, 1/1000), goat anti-mouse IgG3-AP (cat# 1100-04, 1/1000), goat anti-mouse IgE-AP (cat# 1110-04, 1/1000)

For confocal microscopy following antibodies were used: rat anti-mouse IgG2b–FITC (R12-3, BD Pharmingen, cat# 553395, 1/200), rat anti-mouse IgD–PE (11-26c.2a, BD Pharmingen, cat# 558597, 1/600), rat anti mouse B220-eF615 (RA3-6B2, eBioscience (ThermoScientific), cat# 42-0452-82, 1/400), rat anti-mouse CD4–AF700 (GK1.5, eBioscience (ThermoScientific), cat# 56-0041-82, 1/200), rat anti-mouse CD19-APC (1D3, BD Pharmingen, cat# 561738, 1/200), rat anti-mouse CD49f-eF450 (eBioGoH3, eBioscience (ThermoFisherScientific), cat# 48-0495-82, 1/200), rat anti-mouse CD45-AF700 (30-F11, eBioscience (ThermoFisherScientific), cat# 56-0451-82, 1/200), rat anti-mouse CD4-eF570 (RM4-5, eBioscience (ThermoFisherScientific), cat# 41-0042-82, 1/200), rat anti-mouse CD35-BV510 (8C12, BD OptiBuild, cat# 740132, 1/500), rat anti-mouse CXCR5-AF647 (L138D7, BioLegend, cat# 145531, 1/100), hamster anti-mouse PD-1-BV421 (J43, BD Horizon, cat# 562584, 1/200), rat anti-mouse HEV-AF488 (MECA-79, eBioscience, cat# 53-6036-82, 1/200), rat anti-mouse Lyve-1-eF615 (ALY7, eBioscience, cat# 42-0443-82, 1/200), rat anti-mouse CXCL13-APC (DS8CX13, eBioscience, cat# 17-7981-82, 1/200), rat anti-mouse Langerin (CD207)–AF488 (929F3.01, Dendritics, cat# DDX0362A488-100, 1/200).

Validation

All antibodies are commercially available (cataloge numbers provided above). Each reagent handled as per manufacturers instructions, however, concentration for each antibody was determined through titration test prior the actual experiment. Titration was performed to assess the best signal-to-noise ratio. Each antibody was tested for each tissue type prior determining the optimal concentration for the entire experiment. It is important to note that skin tissues often required slightly higher concentration of antibody than LN, in such instances the optimal skin staining was prioritized. Titration was performed for each new antibody at a range of concentrations from 1/50 to 1/1000. Data were then acquired on FACS analyzer and evaluated using FlowJo software prior the actual experiment.

Animals and other research organisms

Policy information about studies involving animals; ARRIVE guidelines recommended for reporting animal research, and Sex and Gender in Research

Laboratory animals

Germ-free C57BL/6NTac mice were bred and maintained in the National Institute of Allergy and Infectious Diseases (NIAID) Microbiome Program gnotobiotic animal facility. C57BL/6 specific pathogen-free (SPF) mice were purchased from Taconic. C57BL/10SgSnAi-[KO]UMT (μMT), C57BL/6-[Tg]CD11c:EYFP (CD11c-YFP), C57BL/6-[KO]CCR7 (Ccr7-/-) mice were obtained through the NIAID-Taconic exchange program. Il21r-/- mice were generously provided by Dr. Warren Leonard (NHLBI/NIH), Bcl6floxCd4cre mice were kindly provided by Dr. Pamela Schwartzberg (NIAID/NIH), Cd40lg-/- mice were kindly provided by Dr. Joseph Kovac (NIH), Ltα-/- mice were generously provided by Dr. Vanja Lazarevic (NCI/CCR/NIH), huLang-DTR mice were kindly provided by Dr. Daniel Kaplan (University of Pittsburgh), Aicda-/- mice were generously provided by Dr Christian Mayer (NCI/NIH). Cd19cre (jax# 006785), Prdm1flox (jax# 008100), Foxp3EGFP-cre-ERT2 (jax# 016961), Rosa26tdTomato (jax# 007909) and AID-GFP (jax#: 018421) were purchased from Jackson Laboratories. Bcl6-YFP mice were provided by Dr. David Dominguez-Sola (Mount Sinai, NYC). All mice were bred and maintained under pathogen-free conditions at an American Association for the Accreditation of Laboratory Animal Care (AAALAC)-accredited animal facility at the NIAID and housed following the procedures outlined in the Guide for the Care and Use of Laboratory Animals (temperature - from +20 to +24oC, humidity - 30-70%, 14 hours light/10 hours dark). All experiments were performed at the NIAID under an animal study proposal (LHIM-3E) approved by the NIAID Animal Care and Use Committee. Gender- and age-matched mice between 6 and 12 weeks of age were used for each experiment. When possible, preliminary experiments were performed to determine requirements for sample size, considering resources available and ethical, reductionist animal use. Each mouse of the different experimental groups is reported (see 'n' in figure legends). Exclusion criteria such as inadequate staining or low cell yield due to technical problems were pre-determined. Animals were assigned randomly to experimental groups.

Wild animals

Wild animals were not involved in this study.

Reporting on sex

Reported experimental phenotypes were reproduced in both genders as part of the repeat experiments, but gender-related differences in terms of the magnitude of the response between male and female treated groups were observed. For this reason, each experiment contained same gender control as experimental groups.

Field-collected samples

Field-collected samples were not used in this study.

Ethics oversight

All experiments were performed at the NIAID under an animal study proposal (LHIM-3E) approved by the NIAID Animal Care and Use Committee. When possible, preliminary experiments were performed to determine requirements for sample size, considering resources available and ethical, reductionist animal use.

Note that full information on the approval of the study protocol must also be provided in the manuscript.

Plants

Seed stocks	Plants were not used for this study
Novel plant genotypes	Not applicable
Authentication	Not applicable

Flow Cytometry

Plots

Confirm that:

☒ The axis labels state the marker and fluorochrome used (e.g. CD4-FITC).

☒ The axis scales are clearly visible. Include numbers along axes only for bottom left plot of group (a 'group' is an analysis of identical markers).

☒ All plots are contour plots with outliers or pseudocolor plots.

☒ A numerical value for number of cells or percentage (with statistics) is provided.

Methodology

Sample preparation	Single-cell suspension was prepared from murine skin and lymph nodes (cell extraction process described in the methods section). Cells were stained with LIVE/DEAD Fixable Blue Dead Cell Stain Kit (Invitrogen) in PBS for 30 min at +4oC to exclude dead cells. Samples were washed 3 times and blocked for 15 min on ice in PBS/0.1%BSA supplimented with FcBlock (Thermofisher), 0.2 mg/ml purified rat IgG, and 1 mg/ml of normal mouse serum (Jackson Immunoresearch) to avoid unspecific binding . Cell suspension was washed and surface staining was added in the blocking buffer for 45 min on ice (in dark) with antibodies specificed above, i.e., TCRβ (H57-597), CD4 (RM4-5 or GK1.5), CD62L(MEL-14), CD45 (30-F11), CD24 (M1/69), CXCR5 (L138D7), PD-1 (J43), IgD (11-26c.2a), IgG1 (A85-1), IgG2b (R12-3), B220 (RA3-6B2), CD19 (1D3 or 6D5), GL-7 (GL7), CD38 (90), CD95 (Jo2), MHCII (M5/114.15.2), CD11b (M1/70), CD11c (N418), CD44 (IM7), CD103 (M290), XCR1 (ZET), F4/80 (BM8), and CD25 (PC61.5). After the surface staining cells were washed 3 times in PBS and fixed in PFA for 1h at room temperature in dark. After fixation, cells were washed again 3 times and resulting cell pellets were permeabilized and stained with intracellular antibodies in saponin containing buffer for 1h at room temperature in dark. For the detection of transcription factors, i.e., BCL6 (K112-91), ki-67 (SolA15), Foxp3 (FJK-16s), cells were fixed and stained using the Foxp3 staining set (ThermoFisher Scientific) according to the manufacturer's protocol. For detection of langerin (CD207) expression, cells were fixed with BD Cytofix/Cytoperm and stained in BD Perm Wash buffer (BD Biosciences). After intracellular staining cells were washed 3 times and acquired on BD LSRFortessa cell analyzer (BD Biosciences).
Instrument	For immune cell phenotyping BD LSRFortessa cell analyzer (BD Biosciences); for cell sorting FACSAria Fusion cell sorter (BD Biosciences) was used.
Software	Analyzer was equipped with FACSDiva software (v9.0). Acquired data were analyzed using FlowJo software (v10.8.2)
Cell population abundance	In the skin compartment B cells are not the most abundant population, but among all CD45-expressing cells B cells reconstitute about 1-5% of population at homeostasis. In contrast, in LN, B cells compose over 30% of all CD45+ cells. After S.epidermidis topical association, skin B cell population slowly increases to as much as 20% of all CD45+ cells 45 days post-association, but even that gives only about 5 000 cells/ear skin. A major drawback is the harsh tissue digestion prior to the cell phenotyping assay that either won't allow for all cells to be extracted or may kill some cells on the way. For this reason it has been extremely hard to extract sufficient cell numbers for downstream analysis (sequencing) and hence it has been easier to study B cell biology via imaging approaches. Total number of cells per population extracted from skin tissue is provided in the supplementary figures.
Gating strategy	Gating strategies for sorting and identification of Treg/TFH/TFR populations are provided in Extended Data Figure 2, but for Langerhans cell identification in Extended Data Fig. 6. However, gating for all cell populations starts the same - we first identify "approximate" lymphocyte population drawing a generous gate on ungated cells displayed on SSC-A and FSC-A axes. Then we subgate to select for singlets based on FSC-H and FSC-W axes. After that we subgate to identify live cells based on negative staining for LIVE/DEAD Fixable Blue Dead Cell Stain. Then, among live cells we subgate for CD45-expressing cells based on CD45 and SSC-A axes. Then, among CD45 cells we identify CD4+ T cells (TCRb+CD4+ double positive). From double negative population we select for double positive B220+CD19+ B cells, while double negative gate B220-CD19- is then further processed for myeloid populations (Extended Data fig. 6). Among B cells we then gate for IgD negative cells and among those we identify germinal center B cells that express GL7, but are negative for CD38 (see figure 3). GL7+ cells also express Bcl6, ki-67, CD95.

Whenever new antibody is used in the panel FMO controls are prepared to identify positive and negative gates for the population.

☒ Tick this box to confirm that a figure exemplifying the gating strategy is provided in the Supplementary Information.